ATLAS NOTE

ATLAS-CONF-2016-018

24th March 2016

Search for resonances in diphoton events with the ATLAS detector at $\sqrt{s}$=13 TeV

The ATLAS Collaboration

Abstract

Searches for new resonances decaying into two photons in the ATLAS experiment at the LHC are described. The analysis is based on pp collision data corresponding to an integrated luminosity of 3.2 fb^{-1} at $\sqrt{s}$=13 TeV recorded in 2015. Two different searches are performed, one targeted for a spin-2 particle, using Randall-Sundrum graviton states as a benchmark model, and one optimized for a spin-0 particle. The most significant deviation from the background predictions is observed at a diphoton invariant mass around 750 GeV with local significances of 3.6 and 3.9 standard deviations in the searches optimized for a spin-2 and spin-0 particle, respectively. The global significances are estimated to be 1.8 and 2.0 standard deviations. The consistency between the data collected at 13 TeV and 8 TeV is also evaluated. Limits on the production cross-section for the two benchmark resonances are reported.

1 Introduction

Searches are described for new high-mass resonances decaying into two photons using LHC proton-proton (pp) collision data at $\sqrt{s}$= 13 TeV recorded in 2015 by the ATLAS detector. The data correspond to an integrated luminosity of 3.2 fb^{-1}. New high-mass states decaying into two photons are predicted in many extensions of the Standard Model (SM). The diphoton final state provides a clean experimental signature with excellent invariant mass resolution and moderate backgrounds.

The spin of the hypothetical particle, which is assumed to be 0 or 2 in the following, causes significant differences in the kinematics of the decay photons. These are exploited by applying two different selections, with looser selection cuts for a spin-2 resonance search. However, the photon identification criteria and the event pre-selection are common in both searches.

The search for a spin-2 $\gamma\gamma$ resonance uses the Randall-Sundrum (RS) model [1] graviton as a benchmark. This entails a lightest Kaluza-Klein [2] spin-2 graviton excitation (G^*) with a dimensionless coupling $k/\overline{M}_{\mathrm{Pl}}$, where $\overline{M}_{\mathrm{Pl}} = M_{\mathrm{Pl}}/\sqrt{8\pi}$ is the reduced Planck scale and k the curvature scale of the extra dimension. The lightest graviton excitation is expected to be a fairly narrow resonance for $k/\overline{M}_{\mathrm{Pl}}< 0.3$ [3], with the width given by $1.44(k/\overline{M}_{\mathrm{Pl}})^2 m_{G^*}$. For $k/\overline{M}_{\mathrm{Pl}} = 0.1$, the natural width increases from 11 GeV at m_{G^*} = 800 GeV to 30 GeV at m_{G^*} = 2200 GeV. For m_{G^*} = 800 GeV, the effects of the natural width and of the experimental mass resolution are comparable. In order to perform the search up to the highest invariant masses where a small number of data events is expected, the shape of the invariant mass distribution of the main background from production of prompt photon pairs is estimated from theoretical computations, and the contribution from the reducible background of jets misidentified as photons is added from data-driven estimates. This analysis is performed in the mass range 500-3500 GeV and in the $k/\overline{M}_{\mathrm{Pl}}$ range 0.01 to 0.3, searching for an excess modelled by the RS graviton resonance shape convolved with the experimental resolution over the estimated background diphoton invariant mass distribution.

Spin-0 $\gamma\gamma$ resonances are predicted in theories with an extended Higgs sector [4–10]. The search for a spin-0 resonance uses a restricted kinematic range, taking advantage of the isotropic distribution of the decay products in the centre-of-mass frame of the new particle. The background is estimated by fitting the diphoton invariant mass distribution to an analytical function, searching for an excess modelled by a spin-0 resonance convolved with the experimental resolution. The search is performed in the mass range 200-2000 GeV where there are enough data to constrain the background shape and for width values up to 10% of the mass of the hypothesized particle.

Searches for diphoton resonances in LHC Run-1 data have been reported by the ATLAS and CMS collaborations [11–16]. First results from high-mass diphoton resonances from 13 TeV pp collision data are reported in Refs. [17, 18]. The search for a spin-0 resonance described in this note follows closely the analysis described in Ref. [17]. In the present study, the significance scan is extended to cover a broad range of hypothesized masses and widths with more accurate signal parametrizations and improved estimates of the modelling uncertainties. In addition, the compatibility with the 8 TeV data is studied after applying the latest photon energy calibration available for the 8 TeV data.

The note is organized as follows: after a description of the data and simulated event samples in Section 2, the photon selection and energy measurements are presented in Section 3. In Sections 4 to 7 the event selection, the modelling of the signal and the estimation of the background as well as the statistical procedure to analyze the data are presented. The results are discussed in Section 8.

2 Data and simulated event samples

Data were collected by the ATLAS detector [19] in 2015 using pp collisions at a centre-of-mass energy of $\sqrt{s}$ = 13 TeV with a bunch spacing of 25 ns, an average number of pp interactions per bunch crossing of about 13, and a peak instantaneous luminosity of L = 5 $\cdot 10^{33}$ cm^{-2}s^{-1}. Events from pp collisions were recorded using a diphoton trigger with transverse energy $E_\text{T} = E \sin(\theta)$ [1] thresholds of 35 GeV and 25 GeV for the E_T-ordered leading and subleading photon candidates, respectively. In the high-level trigger, clusters of energy in the electromagnetic calorimeter are reconstructed and required to satisfy loose criteria according to expectations for showers initiated by photons. The trigger has a signal efficiency close to 99% for events fulfilling the final event selection. Only events taken in stable beam conditions, and in which the trigger system, the tracking devices and the calorimeters were fully operational, are considered. After data-quality requirements, the data sample corresponds to an integrated luminosity of 3.2 fb^{-1}. The measurement of the integrated luminosity has an uncertainty of ±5%. It is derived, following a methodology similar to that detailed in Ref. [20], from a preliminary calibration of the luminosity scale using van der Meer scans performed in August 2015.

Simulated Monte Carlo (MC) samples are used to optimize the search strategy and to check the background estimates. Interference effects between signal and background processes are neglected. Signal samples for the RS graviton model are generated using Pythia8 [21] with parton distribution functions (PDF) NNPDF23LO [22] and the underlying-event tune A14 [23], for different choices of the graviton mass and the parameter $k/\overline{M}_\text{Pl}$, spanning a mass range from 500 GeV to 5 TeV and $k/\overline{M}_\text{Pl}$ values from 0.01 to 0.3. Only the lowest mass RS graviton state is generated. Samples for any mass or $k/\overline{M}_\text{Pl}$ value can be obtained by properly reweighting a large event sample generated with a flat mass distribution, taking into account both the Breit-Wigner term and the parton luminosity terms. The validity of this procedure is verified using samples generated at discrete values of m_{G^*} and $k/\overline{M}_\text{Pl}$. Because the graviton coupling increases with the energy of the decay products, the invariant mass distribution for a large-width graviton signal exhibits a high-mass tail which is not present for a spin-0 Higgs-like particle.

The signal in the spin-0 particle search is simulated using a SM Higgs-like boson produced in pp collisions via gluon fusion and decaying into two photons. Other production processes are investigated to assess the impact of the production mode on the signal modelling. MC samples are produced for different hypotheses of the spin-0 boson mass (m_X) in the range 200 to 2000 GeV and of the decay width (Γ_X) up to 10% of m_X. For the narrow width approximation (NWA), the width of the particle is set to 4 MeV. Gluon fusion events are generated with Powheg-box [24, 25] interfaced with Pythia8 for the underlying event, parton showering and hadronization. To model signals with large decay widths, a function parameterizing the theoretical line-shape of the resonance is used [26, 27]. The Powheg-box implementation of a large-width spin-0 resonance with SM-like couplings is chosen for this function. The line-shape is modelled with a Breit-Wigner distribution based on a running-width scheme, including the dependence of the cross section on the gluon-gluon parton luminosity. In order to reduce modelling effects from the off-shell region, the sample generation is restricted to the region $m_X \pm 2\Gamma_X$. The validity of this procedure is checked by comparing the result of this implementation with simulated samples generated with a large width in Powheg. Events produced via vector boson fusion are generated using Powheg-box [28] interfaced with Pythia8. Associated production with a vector boson or a $t\bar{t}$ pair is generated with Pythia8. The

---

[1] The ATLAS experiment uses a right-handed coordinate system with its origin at the nominal interaction point (IP) in the centre of the detector and the z-axis along the beam pipe. The x-axis points from the IP to the centre of the LHC ring, and the y-axis points upward. Cylindrical coordinates (r, ϕ) are used in the transverse plane, ϕ being the azimuthal angle around the z-axis. The pseudorapidity is defined in terms of the polar angle θ as $\eta = - \ln \tan(\theta/2)$.

CT10 [29] PDF set is used for the samples generated with Powheg-box, while CTEQ6L1 [30] is used for the samples generated with Pythia8. The underlying-event generation for the gluon fusion and vector boson fusion samples is based on the Pythia8 AZNLO tune [31], while for the other samples, the A14 tune is used.

Events containing two prompt photons with up to two additional partons, representing the largest irreducible background to the search, are simulated using the Sherpa [32] generator. The gluon-induced box process is also included. Samples of the photon+jet reducible background component are also generated using Sherpa. The CT10 PDF set is used in conjunction with a dedicated parton-shower tune of Sherpa. Pythia8 is also used to generate Standard Model diphoton production based on the leading order quark-antiquark t-channel annihilation diagram and the gluon-induced box process.

The generated events are passed through a full detector simulation [33] based on Geant4 [34]. Pileup from additional pp collisions in the same and neighbouring beam crossings is simulated by overlaying each MC event with a variable number of simulated inelastic pp collisions generated using Pythia8 with the AZNLO tune. The MC events are weighted to reproduce the distribution of the average number of visible interactions per bunch crossing observed in the data.

3 Photon selection

Photon and electron candidates are reconstructed from clusters of energy deposited in the electromagnetic calorimeter. Candidates without a matching track or reconstructed conversion vertex in the inner detector are classified as unconverted photon candidates. Those with a matching reconstructed conversion vertex or a matching track, consistent with originating from a photon conversion are classified as converted photon candidates. Those matched to a track consistent with originating from an electron produced in the beam interaction region are kept as electron candidates.

Only photon candidates with $|\eta| < 2.37$ are considered, not including the transition region $1.37 < |\eta| < 1.52$ between the barrel and end-cap calorimeters. The calorimeter granularity in the transition region is reduced, and the presence of significant additional inactive material affects the identification capabilities and energy resolution.

Photon identification is based primarily on shower shapes in the electromagnetic calorimeter [35], with the selection criteria re-optimized for the conditions expected for the 2015 data. A loose selection is derived using only the information from the hadronic calorimeter and the lateral shower shape in the second layer of the electromagnetic calorimeter, which contains most of the energy. The final tight selection applies tighter criteria on these variables, different for converted and unconverted photon candidates. It also puts requirements on the shower shape in the finely segmented first calorimeter layer to ensure the consistency of the measured shower profile with that originating from a single photon impacting the calorimeter. When applying the photon identification criteria on simulated events, the shower shapes are corrected for the small differences in their average values between data and simulation. The efficiency of the photon identification increases with E_T from 85% at $E_T = 50$ GeV to 95% at $E_T = 200$ GeV. For $E_T > 50$ GeV, the uncertainty on the photon identification efficiency varies between ±1% and ±5% depending on η and E_T. This uncertainty is estimated from the impact of the differences between data and simulation on the shower-shape variables. This procedure was found to provide a conservative estimate of the uncertainties measured with the 8 TeV collision data collected in 2012 [35].

To further reject the background from jets misidentified as photons, the photon candidates are required to be isolated using both calorimeter isolation and track isolation requirements. The calorimeter isolation variable, E_T^{iso}, is defined as the sum of the E_T of energy clusters deposited in a cone of size $\Delta R = \sqrt{(\Delta \eta)^2 + (\Delta \phi)^2} = 0.4$ around the photon candidate, excluding an area of size $\Delta \eta \times \Delta \phi = 0.125 \times 0.175$ centered on the photon cluster; the expected photon energy deposit outside the excluded area is subtracted. The pileup and underlying event contribution to the calorimeter isolation variable is subtracted from the isolation energy event-by-event [36]. The selection on the calorimeter isolation variable is defined by $E_T^{iso} < 0.022 E_T + 2.45$ GeV, where E_T is the transverse energy of the photon candidate. The track isolation variable (p_T^{iso}) is defined as the scalar sum of the transverse momenta of the tracks in a cone of $\Delta R = 0.2$ around the photon candidate. The tracks are required to have $p_T > 1.0$ GeV and to be consistent with originating from the diphoton primary vertex, defined in the next section. For converted photons, the one or two tracks associated with the photon conversion are excluded from the p_T^{iso} computation. The requirement applied on the track isolation variable is $p_T^{iso} < 0.05 E_T$.

The efficiency of the isolation requirements is studied using several data control samples. Electrons from Z-boson decays are used to validate the isolation variables up to $E_T = 100$ GeV. Inclusive photon samples are used to check the efficiency of the isolation requirement in a wide E_T range from 50 GeV up to 1 TeV. When investigating the distribution of the isolation variables for inclusive photons fulfilling the tight identification selection, the remaining background from jets misidentified as photons is estimated using control samples with a subset of the tight identification requirements inverted. It is then normalized to the selected candidates fulfilling tight identification requirements with very large values of the isolation variable ($E_T^{iso} - 0.022 E_T > 12$ GeV in the case of the calorimeter isolation), for which the signal contribution is expected to be negligible. From this procedure, small differences between data and simulation in the average calorimeter isolation variable are observed as a function of E_T and η of the photon candidates. The size of this difference is used as a systematic uncertainty. A similar procedure is also employed to check the efficiency of the track isolation criteria, with the background-subtracted distribution being used to compute the efficiency in data. The difference in the efficiency between data and simulation is taken as the systematic uncertainty for the track isolation requirement efficiency. Figure 1 shows an example of the comparison of the calorimeter isolation variable for inclusive photons in the E_T range from 125 GeV to 145 GeV for different η intervals. A difference in some η regions between the background-subtracted data and the prediction of the simulation is observed which is likely related to systematic uncertainties in the background subtraction in the inclusive photon sample.

The measurement of the electron or photon energy is based on the energy collected in calorimeter cells in an area of size $\Delta \eta \times \Delta \phi$ of 0.075×0.175 in the barrel and 0.125×0.125 in the end-caps. A multivariate regression algorithm [37] to calibrate electron and photon energy measurements was developed and optimized on simulated events. Corrections are made for the energy deposited in front of the calorimeter and outside of the cluster, as well as to account for the variation of the energy response as a function of the impact point on the calorimeter. The inputs to the energy calibration algorithm are the measured energy per calorimeter layer, including the presampler, the η of the cluster and the local position of the shower within the second-layer cell corresponding to the cluster centroid. In addition, for converted photons, the track transverse momenta and the conversion radius are used as inputs to the regression algorithm to further improve the energy resolution, especially at low energy. The calibration of the input layer energies in the calorimeter is based on the measurement performed with 2012 data [37]. The overall energy scale in data, as well as the difference in the constant term of the energy resolution between data and simulation, are estimated with the sample of Z-boson decays to electrons recorded in 2012 and reprocessed using the same conditions as used for the 2015 data taking and event processing. At E_T values larger than 100–
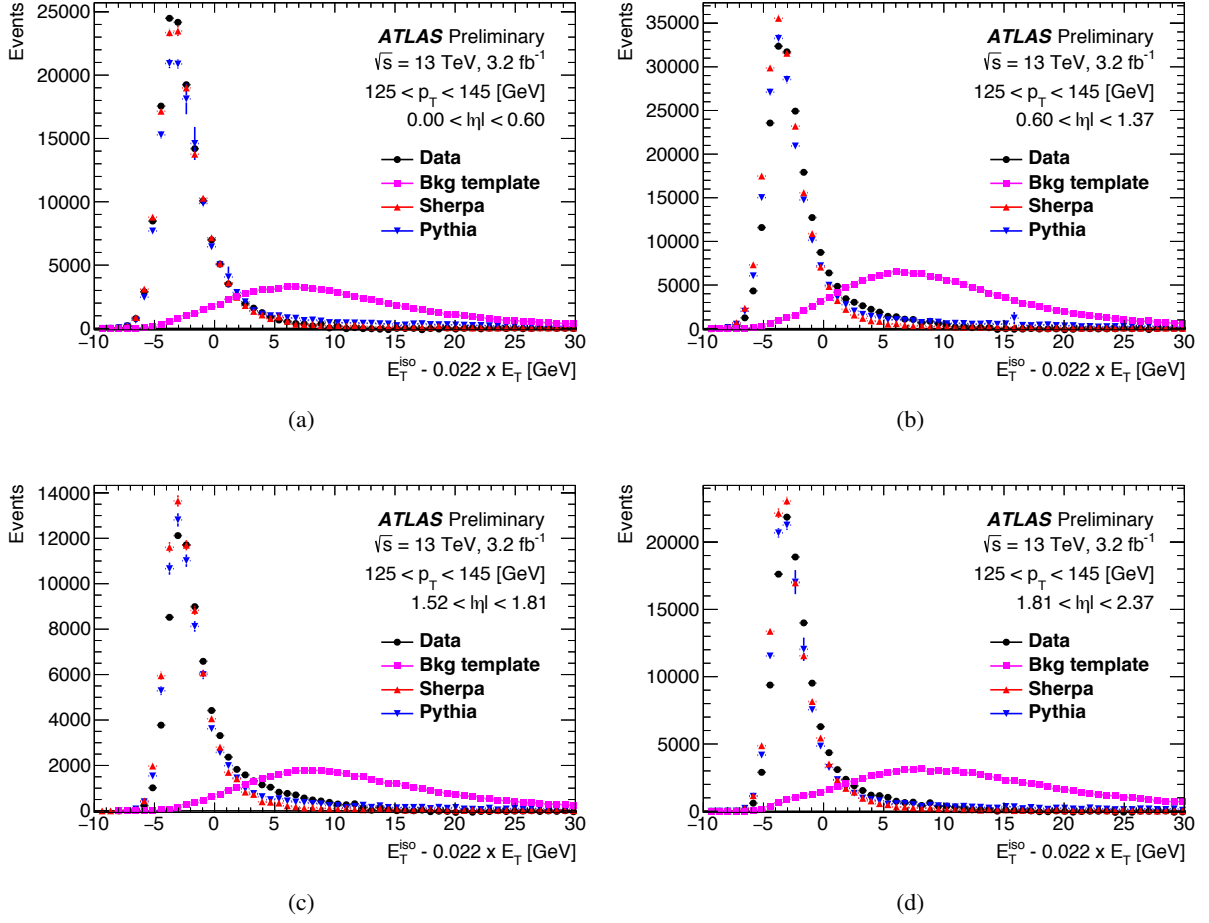
Figure 1: Distributions of the calorimeter isolation variable ($E_T^{iso} - 0.022E_T(\gamma)$) for photon candidates fulfilling the tight identification criteria for 125 GeV $< E_T <$ 145 GeV and four η regions. The background contribution to the data, shown as "Bkg template", has been subtracted using a control sample with a subset of the identification requirements inverted and normalized to the data above 12 GeV for $E_T^{iso} - 0.022E_T(\gamma)$. The data distributions are compared to predictions from simulation using either SHERPA or PYTHIA8 to generate inclusive photon events. Only statistical uncertainties are shown in the subtracted data distributions. The calorimeter isolation requirement corresponds to a cut at 2.45 GeV on this variable.

200 GeV, the energy resolution is dominated by the constant term of the calorimeter energy resolution, which amounts to $0.6\% - 1.5\%$ depending on η. In addition to the uncertainties on the energy calibration with the 2012 data [37], additional uncertainties (typically $0.2 - 0.3\%$ on the energy scale and 0.5% absolute on the constant term) account for the extrapolation from the 2012 dataset to the 2015 dataset. This extrapolation uncertainty mostly affects the uncertainty on the constant term. The energy scale and resolution corrections are checked using Z-boson decays to electrons recorded in the 2015 dataset and are found to be valid within their uncertainties. The uncertainty on the photon energy scale at high E_T is typically $\pm(0.5\text{-}2.0)\%$ depending on η, and the preliminary relative uncertainty on the photon energy resolution for $E_T = 300$ GeV is between $\pm80\%$ and $\pm100\%$ depending on η. Additional uncertainties related to the extrapolation of the energy scale to photons of very high energies, in addition to those described in Ref. [37], have been considered and found to be small. In particular, detailed checks of the

validity of the calibration for the lowest gain range of the electronics readout [38] of the electromagnetic calorimeter, which is used in the E_T range above 350 GeV in the central part of the electromagnetic barrel calorimeter, have been performed, including checks with high-E_T electrons from Z-boson decays. These checks show that the relative calibration of the low-gain readout with respect to the other gains is better than ±1%.

4 Event selection and sample composition

Starting from the triggered events, two photon candidates fulfilling the tight identification requirements are required, with E_T above 40 GeV and 30 GeV. The primary vertex corresponding to the pp collision that produced the diphoton candidate is identified. In addition, the calorimeter and the track isolation requirements are applied to further reduce the background from jets misidentified as photons, thus increasing the expected sensitivity of the analyses. Different additional selections are then applied, separately in the search for a spin-2 or spin-0 resonance.

4.1 Primary vertex selection

The mass reconstruction requires the reconstructed primary vertex corresponding to the pp collision that produced the diphoton candidate. The correct identification of the tracks coming from the pp collision producing the diphoton candidate is also necessary to avoid pileup contributions to the track isolation. To keep the contribution of the opening angle resolution to the mass resolution smaller than the contribution of the energy resolution, a position resolution for the primary vertex of about 15 mm in the z-direction is required. An even better resolution is needed to correctly match tracks to the pp collision vertex of the diphoton candidate. The directions of both photon candidates are measured based on the longitudinal and transverse segmentation of the electromagnetic calorimeter, with a resolution of about 60 mrad/$\sqrt{E}$, where E is the photon energy in GeV. An estimate of the z-position of the diphoton primary vertex is obtained by combining the average beam-spot position with this photon pointing. It may be enhanced using the tracks from photon conversions with conversion radii before or in the volume of the silicon detectors. This estimate gives a resolution of about 15 mm in the z-direction. In order to select the best primary vertex for the diphoton event, a neural-network discriminant, similar to the one used in Ref. [39], is constructed using both the z-position of the diphoton primary vertex estimated by the photon pointing including its uncertainty and additional information from the tracks associated to each reconstructed primary vertex. After applying this procedure, the contribution of the opening angle resolution to the mass resolution is negligible. The efficiency to reconstruct the correct primary vertex within ±0.3 mm is about 88%.

4.2 Event selection

In the selection used to search for a spin-2 resonance, the transverse energy of each photon is required to be $E_T > 55$ GeV. With this selection, 5066 diphoton events with diphoton invariant mass $m_{\gamma\gamma} > 200$ GeV are selected in the data.

The search for a spin-0 resonance applies tighter selections which have been optimized on simulated background and signal samples to enhance the sensitivity to a spin-0 particle. Given the isotropic distribution of the decay, the transverse energies of the two photons are expected to be higher than those of

photons from background processes. The transverse energy is required to be $E_T > 0.4m_{\gamma\gamma}$ for the photon with the highest E_T and $E_T > 0.3m_{\gamma\gamma}$ for the photon with the second-highest E_T, for a given value of $m_{\gamma\gamma}$. This selection improves the expected sensitivity by more than 20% for masses larger than 600 GeV compared to the initial requirement. With these requirements, 7391 (2878) events are selected in the data with $m_{\gamma\gamma} > 150$ GeV (> 200 GeV).

4.3 Sample composition

The selected samples are predominantly constituted of events from diphoton production, followed by photon+jet production, with one jet misidentified as a photon, and dijet production with two jets misidentified as photons. The Drell-Yan background, where both electrons are misidentified as photons, is negligible. A quantitative understanding of the sample composition is required for the background estimate in the spin-2 resonance search. It is also used in the studies for the choice of the background function in the spin-0 resonance search.

Methods based on control regions built from events failing the isolation requirement and/or some of the tight photon identification requirements are used to estimate the various sources of background directly from data. Only some of the requirements of the tight photon identification using the first layer of the calorimeter are inverted to minimize the correlation with the isolation variable.

In the first method [40], four regions per photon are constructed, one region corresponding to the signal selection and the others to candidates failing the isolation requirement only, failing part of tight identification requirement only or failing both. For diphoton candidates, 16 control regions are thus obtained. The inputs to the method are the numbers of events in the 16 regions and the signal efficiencies of the tight identification and isolation requirements. The correlation between these two requirements is assumed to be negligible for background events. The method allows the simultaneous extraction of the numbers of genuine diphoton events, photon+jet, jet+photon and dijet background events, and of the efficiencies of the tight identification and isolation requirements for photon candidates from misidentified jets. Photon+jet events correspond to the cases where the sub-leading photon candidate in E_T is a jet misidentified as a photon, and vice-versa for jet+photon events.

The second method [41] classifies the diphoton candidates passing tight identification requirements into four categories depending on whether both, only the leading, only the sub-leading or none of the photons pass the isolation cut. The numbers of observed events in data in these categories are related to the numbers of genuine diphoton, photon+jet, jet+photon and dijet events through isolation efficiencies for signal and background. The efficiency for background is estimated in control regions of the data, using events failing a subset of the tight identification requirements. Events satisfying the tight identification are used to estimate the efficiency for genuine photons, after subtracting the background component, whose amount is estimated by comparing the number of events passing and failing a subset of the tight identification requirements, in a control regions of the data with large track isolation, $p_T^{iso} > 0.05E_T + 10$ GeV. Once these efficiencies are known, the sample composition can be extracted by the inversion of a 4x4 matrix.

Both methods can be applied over the full selected kinematic range, or in bins of $m_{\gamma\gamma}$, thus providing both inclusive and differential yields. Figure 2 shows the decomposition of the selected data sample into the contributions from diphoton, photon+jet or jet+photon, and dijet events for both selections and the corresponding purities, defined as the ratio of diphoton events over the total number of events in the sample. The purity is $(94^{+3}_{-7})\%$ for the spin-2 selection and $(93^{+3}_{-8})\%$ for the spin-0 selection. Uncertainties on these purity estimates come from the statistical uncertainty in the data sample, the definition of the
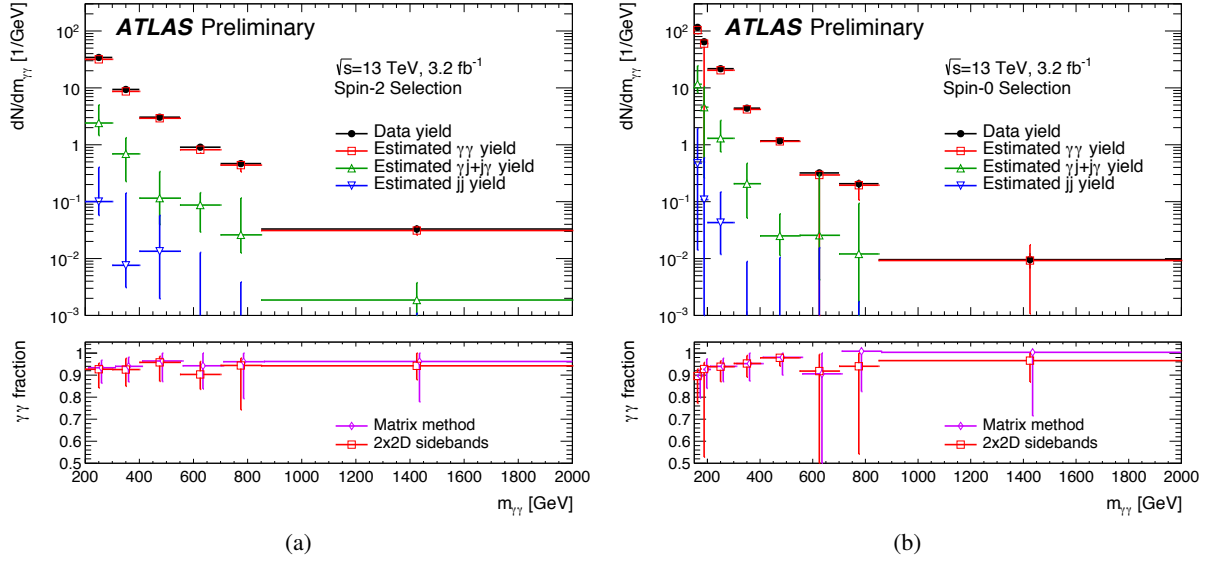
8

Figure 2: The diphoton invariant mass distributions (upper panels) of the data for the spin-2 and spin-0 selections and their decomposition in contributions from genuine diphoton, gamma+jet and jet+jet events as determined using one of the methods described in the text. The bottom panels show the purity of diphoton events as determined from the two methods. The total uncertainties are shown, including statistical and systematic components.

control region failing the tight identification requirement, the modelling of the isolation distribution and possible correlations between the isolation variable and the identification criteria that are inverted. Both methods give consistent results within their uncertainties. The estimate of these uncertainties is sensitive to the small number of events in some of the control regions.

4.4 Signal acceptance and efficiency

The expected signal yield can be expressed as the product of the production cross section times branching ratio to two photons with the acceptance (A) of the kinematic requirements and with the reconstruction and identification efficiency (C). The acceptance is expressed as the fraction of decays satisfying the fiducial acceptance at the generator level. The factor C is defined as the ratio of the number of events fulfilling all the selections applied on reconstructed quantities to the number of events in the fiducial acceptance.

For the spin-2 resonance search, the total value of $A \cdot C$ for the selection ranges from 45% to 60% for masses between 500 GeV and 3 TeV with a small dependence on the width. The uncertainty from the photon identification is about ±3% independent of the mass. The uncertainty from the isolation requirement is ±1% for the calorimeter isolation selection and varies from ±2% for a mass of 500 GeV to ±1% for a mass of 3000 GeV for the track isolation requirement. The uncertainty from the trigger efficiency is ±0.6%. Uncertainties related to photon energy scale and resolution have a negligible impact on the uncertainty on the expected signal yield.

For the spin-0 resonance search, limits are reported in a nearly model-independent way on the fiducial cross section, defined as the product of the cross section times the branching ratio to two photons within the fiducial acceptance. The fiducial acceptance follows closely the selection criteria applied to the

reconstructed data: $|\eta_\gamma| < 2.37$, $E_T > 0.4m_{\gamma\gamma}$ (leading γ), $E_T > 0.3m_{\gamma\gamma}$ (sub-leading γ). An isolation requirement is applied using all particles with lifetime greater than 10 ps at the generator level in a cone of $\Delta R = 0.4$ around the photon direction $E_T^{iso} < 0.05E_T^\gamma + 6$ GeV. The value of the isolation requirement applied at the particle level is adjusted to match the selection applied at the reconstruction level. In addition, for the generator level fiducial acceptance, the generated diphoton invariant mass is required to be within $\pm2\Gamma$ of the resonance mass. The acceptance value ranges from 75% to 85% in the mass range from 200 GeV to 1000 GeV. The reconstruction and identification efficiency C ranges from 55% for an assumed spin-0 particle of mass 200 GeV to 70% for an assumed mass of 1000 GeV. The gluon fusion production mode is used to compute the baseline value of C. Different production modes (vector boson fusion, associated production with W or Z boson or with $t\bar{t}$ pairs) yield differences in C values of at most $\pm3\%$. In the case of a large decay width compared to the detector resolution, the correction factor C varies by up to $\pm5\%$ depending on the assumed decay width. This variation is taken as an additional uncertainty. Other uncertainties on C arise from uncertainties in the trigger efficiency ($\pm0.6\%$), the photon identification efficiency ($\pm3\%$ to $\pm2\%$ depending on the assumed mass) and the photon isolation efficiencies ($\pm4\%$ to $\pm1\%$ depending on the assumed mass). Uncertainties arising from photon energy scale and energy resolution have a negligible impact on C.

5 Signal modelling

The invariant mass distribution of the diphoton pair for the signal is expected to peak near the assumed mass of the new particle, with a spread given by the convolution of its intrinsic decay width with the experimental resolution. For both searches, the invariant mass experimental resolution is modelled with a double-sided Crystal Ball (DSCB) function.

The DSCB function is defined as:

$$
N \cdot \begin{cases}
e^{-t^2/2} & \text{if } -\alpha_{\text{low}} \geq t \geq \alpha_{\text{high}} \\
\dfrac{e^{-0.5\alpha_{\text{low}}^2}}{\left[\dfrac{\alpha_{\text{low}}}{n_{\text{low}}}\left(\dfrac{n_{\text{low}}}{\alpha_{\text{low}}}-\alpha_{\text{low}}-t\right)\right]^{n_{\text{low}}}} & \text{if } t < -\alpha_{\text{low}} \\
\dfrac{e^{-0.5\alpha_{\text{high}}^2}}{\left[\dfrac{\alpha_{\text{high}}}{n_{\text{high}}}\left(\dfrac{n_{\text{high}}}{\alpha_{\text{high}}}-\alpha_{\text{high}}+t\right)\right]^{n_{\text{high}}}} & \text{if } t > \alpha_{\text{high}},
\end{cases} \tag{1}
$$

where $t = \Delta m_X/\sigma_{CB}$, $\Delta m_X = m_X - \mu_{CB}$, N is a normalisation parameter, μ_{CB} is the peak of the Gaussian distribution, σ_{CB} represents the width of the Gaussian part of the function, α_{low} (α_{high}) parametrizes the mass value where the invariant mass resolution distribution becomes a power-law function on the low (high) mass side, n_{low} (n_{high}) is the exponent of this power-law function. For samples with small decay width, the width of the DSCB Gaussian core σ_{CB} parametrizes entirely the effect of the experimental invariant mass resolution.

The diphoton invariant mass resolution for a narrow resonance, as measured by the σ_{CB} parameter, varies from about 2 GeV at a mass of 200 GeV to about 13 GeV at a mass of 2 TeV. The relative uncertainty on the signal mass resolution is mostly driven by the uncertainty on the constant term of the energy resolution, which is the dominant contribution at high energy and varies from $^{+55}_{-20}\%$ to $^{+110}_{-40}\%$ as a function of the mass.

For the spin-2 analysis, the signal mass distribution for any value of the mass and $k/\overline{M}_{\text{Pl}}$ is obtained by a convolution of the intrinsic detector resolution, modelled by a DSCB function, with the predicted mass line-shape distribution at the generator level, as discussed in Section 2. The parameters of the DSCB function

are determined from RS graviton signal samples of various masses with $k/\overline{M}_{Pl} = 0.01$, corresponding to a width of 0.014% times the mass, which is negligible compared to the detector resolution. The convolution approach takes into account the high-mass tail predicted for the benchmark RS graviton model for large coupling values. It is validated by comparing the predicted mass distribution to the one derived in fully simulated samples with different $k/\overline{M}_{Pl}$ values and a good agreement is found.

When considering spin-0 resonances with larger natural widths, simulated as discussed in Section 2, the reconstructed line-shapes for a spin-0 signal are well described by DSCB functions. The function effectively parametrizes the combined effects of the theoretical line-shape and the detector response. The parameters of the DSCB fit function are then expressed as analytical functions of the mass and width of the hypothesized spin-0 resonance. This approach provides an adequate modelling of the signal invariant mass distribution for width values up to 10% of the resonance mass.
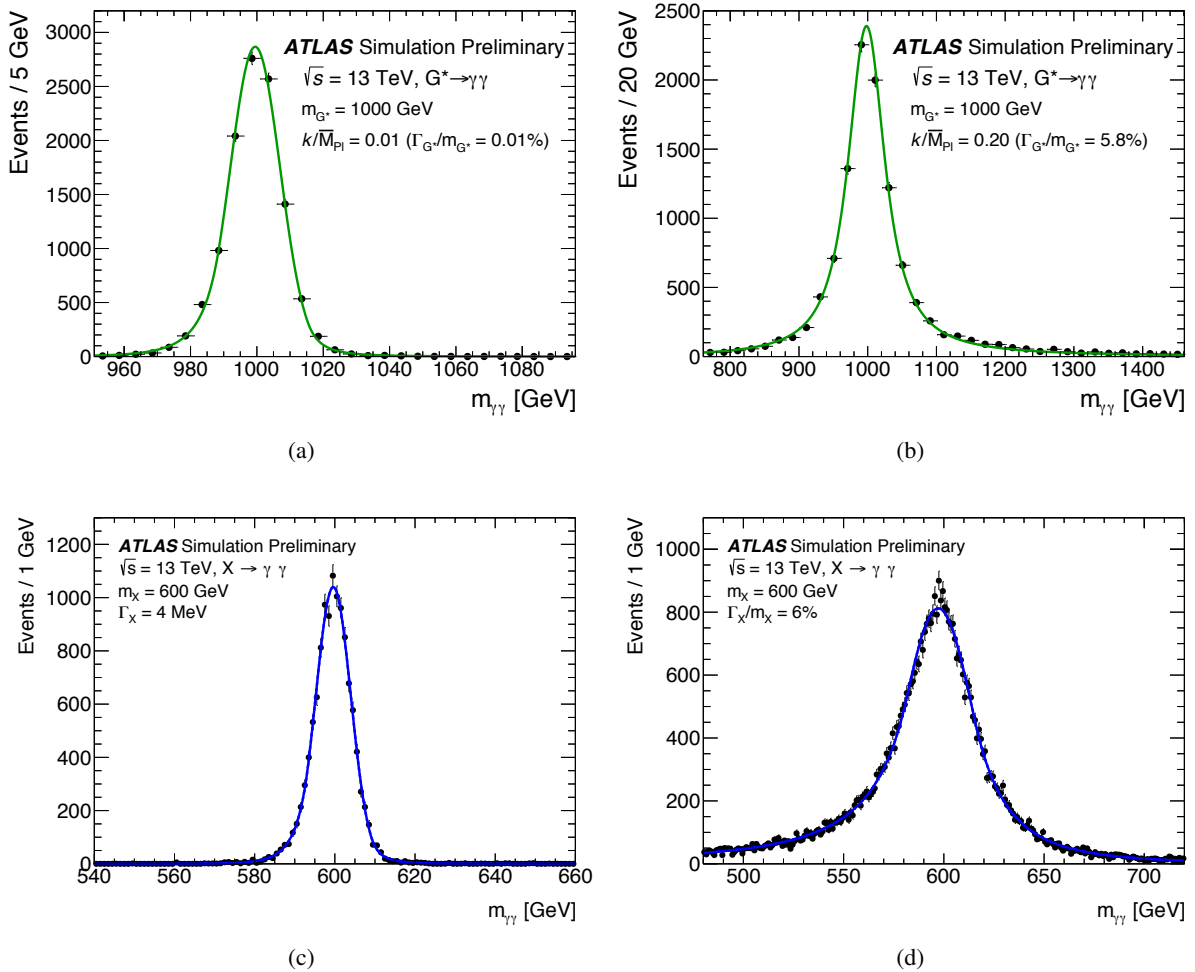
Figure 3: The $m_{\gamma\gamma}$ distributions for different signal hypotheses: RS graviton with mass of 1000 GeV and (a) $k/\overline{M}_{Pl} = 0.01$, (b) $k/\overline{M}_{Pl} = 0.2$, as well as for a scalar resonance with (c) a narrow decay width and with (d) $\Gamma/m = 0.06$. A fit is superimposed using the convolution of the graviton mass line shape with the detector resolution for the graviton signal case and using a double-sided Crystal Ball function for the scalar resonance case.

Figure 3 illustrates the signal modelling for a 1000 GeV RS graviton with $k/\overline{M}_{\mathrm{Pl}} = 0.01$ ($\Gamma_{G^*}/m_{G^*} = 0.01\%$) or 0.2 ($\Gamma_{G^*}/m_{G^*} = 6\%$) and for a 600 GeV scalar particle with either a narrow width or a width equal to 6% of the mass. For both analyses, the bias from the modelling of the signal mass resolution has a negligible impact on the extracted signal yield.

6 Background estimates

Two different methods are used to estimate the continuous background contribution to the $m_{\gamma\gamma}$ distribution. The first approach aims at searching for very high masses, where the small number of data events does not constrain effectively the shape of the invariant mass of the diphoton background. In this approach, the invariant mass shape of the diphoton background is predicted using the fixed order DIPHOX [42] NLO computation. The background from photon+jet and dijet production is added using control samples in the data. This approach is used for the spin-2 resonance search, where the search range is 500-3500 GeV in mass. The second approach is optimized for the mass range in which there are enough data events below and above the investigated resonance mass. An approach based on using a smooth functional form, with fully data-driven parameters to model the total background, thus provides an adequate background estimate. In this approach, used for the spin-0 resonance search, the mass distribution from data is fitted in the range above 150 GeV and the search range for the signal is 200-2000 GeV.

6.1 Monte-Carlo extrapolation approach

The background is separated into the diphoton irreducible component and the reducible contributions from photon+jet and dijet events. To normalize properly each background component, the composition of the data sample in the invariant mass interval 200 GeV to 500 GeV is determined following a procedure similar to that described in Section 4.3. The background shape can then be estimated over the full 200-4000 GeV mass range, taking into account the shapes of each background component and their relative normalizations from the 200-500 GeV range.

The DIPHOX NLO computation is used to predict the shape of the invariant mass distribution of the irreducible diphoton background at the parton level. Kinematic cuts corresponding to the analysis selection ($E_{\mathrm{T}} > 55$ GeV, $|\eta| < 2.37$) are applied. This computation includes the contribution of photons produced in the fragmentation of quarks or gluons. The CTEQ6.6M PDF set [43] is used and the factorization, renormalization and fragmentation scales are set to the mass of the diphoton system. Fully simulated diphoton events generated with SHERPA are reweighted using the ratio between the DIPHOX and SHERPA calculations at the parton level, as a function of the diphoton invariant mass. The reweighting factor varies by about 20% over the diphoton mass range from 200 GeV to 3000 GeV. The uncertainty on the DIPHOX computation is estimated by considering the following effects: uncertainties on the parton density functions (PDF) from variations of the 22 eigenvectors that are provided with the CTEQ6.6M PDF (from ±2% at a mass of 200 GeV up to ±35% at a mass of 3500 GeV on the shape of the normalized invariant mass distribution), on the choice of the PDF set (up to ±5%), on the photon isolation applied at the parton level in DIPHOX (±10%), and on the factorization and renormalization scales in DIPHOX (±10% to ±20%).

To predict the shape of the γ-jet and dijet backgrounds, control samples where one or two of the photons fail the tight identification criteria but fulfill looser selections are used. The shape of the invariant mass

distribution in these control samples is fitted with a function of the form

$$f(m_{\gamma\gamma}) = p_0 \times (m_{\gamma\gamma})^{p_1 + p_2 \log(m_{\gamma\gamma})} \times \left(1 - \frac{1}{1 + e^{(m_{\gamma\gamma} - p_3)/p_4}} \right) \tag{2}$$

where the p_i are free parameters. The uncertainty on the shape of this background is estimated by varying the identification criteria used to select the photons in the control sample.

The uncertainty on the $m_{\gamma\gamma}$ shape of the total background results from the uncertainties on the shape of each component and the uncertainty on the relative normalization of each component. This uncertainty ranges from about ±5% at a mass of 500 GeV to ±35% at a mass of 3.5 TeV. At masses larger than 1 TeV, the main contribution to the uncertainty comes from the shape of the irreducible background which in turn mostly arises from the PDF uncertainty. Figure 4 shows the evolution of the uncertainties on the background prediction as a function of $m_{\gamma\gamma}$ in the region $m_{\gamma\gamma} > 500$ GeV, which is the search range for the spin-2 resonance. The impact of these uncertainties in the range 200 GeV to 500 GeV is also taken into account. Four independent sources of systematic uncertainties are considered, each of them with an impact varying with the invariant mass but fully correlated across the full mass range. These sources are the shape of the reducible background, the relative normalization of the reducible and irreducible backgrounds, the impact of the parton-level isolation requirement in DIPHOX and the effect of the scales and PDF uncertainties on the DIPHOX computation. In addition, MC statistical uncertainties, which are ranging from ±5% to ±10% in a 5 GeV mass interval, are taken into account, uncorrelated from bin to bin.
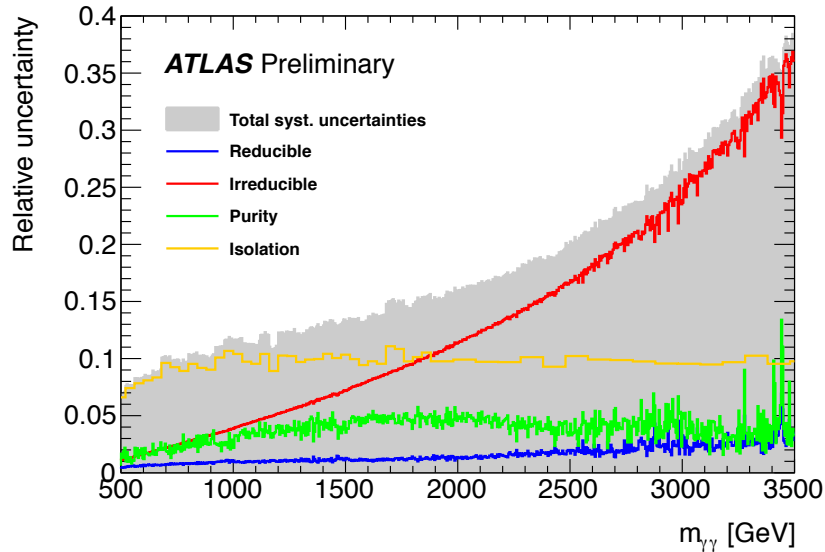
Figure 4: Relative uncertainty on the shape of the $m_{\gamma\gamma}$ distribution of the predicted background for the spin-2 resonance search. The reducible background uncertainty corresponds to the uncertainty on the shape of the reducible background component. The uncertainty on the shape of the irreducible background results from uncertainties affecting the NLO diphoton computation (parton density functions and factorization and renormalization scales). The uncertainty on the purity corresponds to the impact of the relative normalization of the reducible background compared to the irreducible background. The uncertainty on isolation results from the uncertainty in the choice of the parton-level isolation cut in the NLO computation.

13

6.2 Functional form approach

A family of functions, adapted from those used by searches for new physics signatures in dijet final states [44], is chosen to describe the shape of the invariant mass distribution:

$$f_{(k)}(x; b, \{a_k\}) = N(1 - x^{1/3})^b x^{\sum_{j=0}^{k} a_j (\log x)^j} , \qquad (3)$$

where $x = \frac{m_{\gamma\gamma}}{\sqrt{s}}$, k is related to the number of parameters of the function, b and a_k are free parameters, and N is a normalization factor.

To validate the choice of this functional form and to derive the corresponding uncertainties, the method detailed in Ref. [45] is used to check that the functional form is flexible enough to accommodate different physics-motivated underlying distributions. A large sample of diphoton pseudo-data is produced using the DIPHOX NLO computation, where the photon four-vectors are smeared with the detector resolution, and also with SHERPA generated samples which are then passed through the full detector simulation and the event reconstruction. The impact of the PDF uncertainties on the invariant mass distribution is also investigated. The shape of the mass distribution for the reducible γ-jet and dijet backgrounds is estimated with data control samples selected with one or two of the photons failing the tight identification criteria but fulfilling a looser set of requirements. These samples are dominated by events with one or both jets misidentified as photons. As the limited number of data events does not allow directly a precise estimate of the mass distribution for masses above 500 GeV, the invariant mass distribution of these samples is fitted with various smooth functions providing an adequate fit to the data. The final pseudo-data set is obtained by summing the diphoton contribution and the smoothed estimate of the γ-jet and dijet backgrounds. The bias related to the choice of the functional form is estimated as the fitted "spurious" signal yield in these pseudo-data, which consist only of background events, when performing a signal plus background fit for various signal mass hypotheses. To be selected for the analysis the functional form is required to have a fitted "spurious" signal less than 20% of the statistical uncertainty on the fitted signal yield over the full investigated mass range. Among the forms fulfilling this criteria, the one with the lowest number of degrees of freedom is preferred. Based on these criteria, the functional form defined in the equation above with $k=0$ is selected. The uncertainty on the background is estimated from the fitted "spurious" signal. For a narrow signal hypothesis, it varies from 7 events at 200 GeV to 0.006 events at 2000 GeV. For larger hypothesized signal widths, the signal is integrated over a wider mass range and the background uncertainty is larger, from 20 events at 200 GeV to 0.04 events at 2000 GeV, for a hypothesized signal with a width equal to 6% of its mass.

The possibility of needing more degrees of freedom when confronting this functional form with the selected data sample is considered. In order to decide whether a function with increased complexity is needed to describe the data, an F-test is performed. Two background-only fits, using the simplest validated function and a more complex version using a larger value of k, are performed on the selected data, binned according to the expected number of background diphoton events. A test statistic F is computed from the resulting χ^2 values, and its probability is compared with that expected from a Fisher distribution with the corresponding number of degrees of freedom. The hypothesis that the additional degree of freedom is useless is rejected if the probability to have an F value higher than the one observed in the data is less than 5%. The tests do not indicate a need for additional degrees of freedom with respect to the simplest function ($k = 0$).

7 Statistical procedure

The numbers of signal and background events are obtained from maximum likelihood fits of the $m_{\gamma\gamma}$ distribution of the selected events, for (m_X, α) hypotheses where the presence of a spin-0 resonance of mass m_X and width $\Gamma = \alpha m_X$ is probed, or $(m_X, k/\overline{M}_{\text{Pl}})$ hypotheses where a spin-2 resonance from the benchmark RS model is probed.

The function used to describe the data can be written as

$$N_S f_S(m_{\gamma\gamma}) + N_B f_B(m_{\gamma\gamma}), \tag{4}$$

where N_S is the fitted number of signal events, $f_S(m_{\gamma\gamma})$ is the normalized invariant mass distribution for a given signal hypothesis, N_B is the fitted number of background events and $f_B(m_{\gamma\gamma})$ is the normalized invariant mass distribution for the background events. In the spin-2 resonance search, f_B is the sum of the diphoton NLO based computation and the reducible background contribution. In the spin-0 resonance search, f_B is described by a functional form with two free parameters. N_S is related to the assumed signal cross section via the acceptance and detector efficiency correction factors.

Uncertainties on the signal parametrization, the acceptance and detector efficiency correction factors for the signal and on the description of the background shape are included in the fit via nuisance parameters. Uncertainties on the signal modelling are constrained with Gaussian or log-normal penalty terms. In the case of the Monte-Carlo approach, discussed in Section 6.1, the uncertainty on the shape of each background component and on the relative normalization of the different components corresponds to a different nuisance parameter affecting the total background shape, as illustrated in Figure 4. These nuisance parameters are also constrained with Gaussian penalty terms. In the case of the functional form approach, discussed in Section 6.2, for the background estimate, the parameters of the function are nuisance parameters which are completely free in the fit to the data, and the systematic uncertainty on the background description is implemented by the "spurious" signal term, which is constrained by a Gaussian penalty term and, for a given (m_X, α) hypotheses, has the same invariant mass distribution as the signal. This "spurious" signal uncertainty is considered separately for each (m_X, α) hypothesis without any correlation between the different investigated mass ranges.

Every fit allows for a single signal component. The whole mass spectrum (starting at 150 GeV for the spin-0 resonance search and at 200 GeV for the spin-2 resonance search) is used for all probed mass hypotheses.

The local p-value (p_0) for the compatibility with the background-only hypothesis when testing a given signal hypothesis (m_X, α) is based on scanning the $q_0(m_X, \alpha)$ test statistic [46]:

$$q_0(m_X, \alpha) = -2 \log \frac{L(0, m_X, \alpha, \hat{\hat{\nu}})}{L(\hat{\sigma}, m_X, \alpha, \hat{\nu})}, \tag{5}$$

where the values of the parameters marked with the hat superscript are chosen to unconditionally maximize the likelihood, while the value with a double hat is chosen to maximize the likelihood in a background-only fit and ν represents the nuisance parameters which are varied in the fit. This p_0-value is calculated using the asymptotic approximation [46].

Global significance values are computed accounting for the look-elsewhere-effect (LEE). In a first method, which is used for the results given in this note, a large number of pseudo-experiments is generated assuming the background-only hypothesis and, for each pseudo-experiment, a maximum likelihood fit is performed

Uncertainty	spin-2 search	spin-0 search	
Background (mass dependent)	± 7% to ± 35%	spurious signal $20 - 0.04$ events for Γ/M=6%	p_0 and limit
Signal mass resolution (mass dependent)		$(^{+55}_{-20})\% - (^{+110}_{-40})\%$	p_0 and limit
Signal photon identification (mass dependent)		$\pm(3-2)\%$	limit
Signal photon isolation (mass dependent)	$\pm(3-1)\%$	$\pm(4-1)\%$	limit
Signal production process	N/A	$\pm(3-6)\%$ depending on Γ	limit
Trigger efficiency		$\pm0.6\%$	limit
Luminosity		$\pm5.0\%$	limit

Table 1: Summary of systematic uncertainties on the modelling of the invariant mass shape of the background, on the signal mass resolution and on the total signal yield (from uncertainties on photon identification, isolation, process dependence of the reconstruction and identification efficiency C for the spin-0 resonance search, trigger efficiency and integrated luminosity). For mass-dependent uncertainties the quoted ranges cover the range from 500 GeV (200 GeV) to 3500 GeV (2000 GeV) for the spin-2 (spin-0) resonance search. The last column indicates if the corresponding uncertainty affects only the compatibility with the background-only hypothesis (p_0) or also the limit on the signal cross section.

with the signal mass, width and rate as free parameters. The corresponding p_0-value is computed and the global significance is estimated by comparing the minimum p_0-value observed in data to the distribution derived from the pseudo-experiments. A second method, used as cross-check, is based on the techniques described in Refs. [46–48] and used in Ref. [17].

The expected and observed 95% confidence level (CL) exclusion limits are computed using a modified frequentist approach CL_s [49] with the asymptotic approximation [46]. Cross-checks using sampling distributions generated using pseudo-experiments are performed for a few signal mass points and good agreement with the asymptotic approximation is found.

8 Results

Table 1 summarizes the systematic uncertainties used as inputs in the fits. It also indicates whether they affect both the compatibility with the background-only hypothesis and the fitted signal cross-section value or only the fitted signal cross-section value. The uncertainties on the background estimate, discussed in Section 6, and the uncertainties on the shape of the invariant mass distribution of the signal, discussed in Section 5, affect both the compatibility with the background-only hypothesis and the limit on the production cross section of the new resonance. The systematic uncertainty on the background modelling when using the functional form approach is given as the uncertainty on the number of the fitted "spurious" signal yield from imperfect modelling of the background shape. This corresponds to a local relative uncertainty of ± 2% to ±20% as a function of the diphoton mass in the range from 200 GeV to 2000 GeV when converted to a fractional uncertainty on the background rate. For a mass of 750 GeV and a relative width of 6% it amounts to ±8%. For the spin-2 resonance search, the background is estimated using

the Monte-Carlo extrapolation approach discussed in Section 6.1 and the uncertainty on the shape of the background mass distribution is shown in Figure 4. The uncertainties on the normalization of the signal yield, discussed in Section 4.4, affect only the limits on the production cross sections.
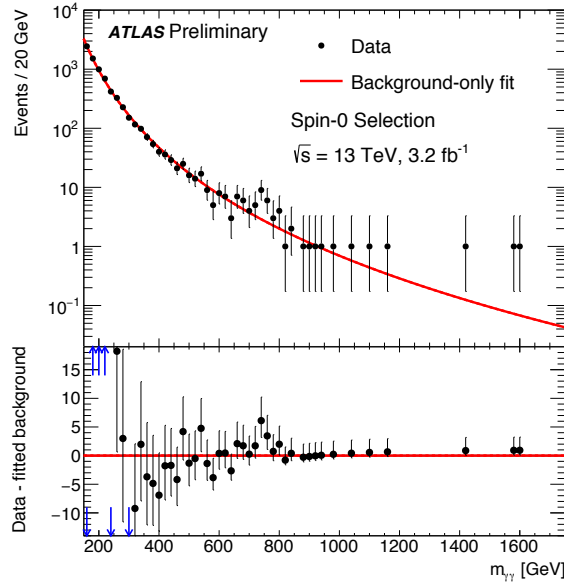
8.1 Results of the search for a spin-0 resonance

Figure 5: Distribution of the invariant mass of the diphoton candidates for the selection used in the search for a spin-0 resonance with the best background-only fit (top). The difference between the data and this fit is shown in the bottom panel. The arrows indicate values outside the range shown in the bottom panel.

Figure 5 shows the diphoton invariant mass distribution for the selection optimized for the spin-0 resonance search together with the best background-only fit (N_S=0).

The compatibility with the background-only hypothesis, quantified with the local p_0-value, is shown in Figure 6 as a function of the hypothesized resonance mass and width for the spin-0 search. For small assumed signal widths, the local significance is slightly overestimated because it does not include the effective additional look-elsewhere effect induced by the resolution uncertainty. This uncertainty is taken into account when estimating the global significance.

The largest deviation is observed near a mass of 750 GeV. It corresponds to a local excess over the background-only hypothesis of 3.9 standard deviations, for a width of ≈ 45 GeV. The global significance evaluated using the search region of $200 - 2000$ GeV in mass and $1\% - 10\%$ in Γ_X/m_X is 2.0 standard deviations. The statistical uncertainty from the number of pseudo-experiments is ±0.1.

The local significance of the excess with floating width reported here, 3.9 standard deviations, is compatible with that reported in Ref. [17], where also a narrow-width fit was performed. The global significance of the floating-width excess reported here is lower than that reported in Ref. [17] due to an improved estimation using pseudo-experiments.
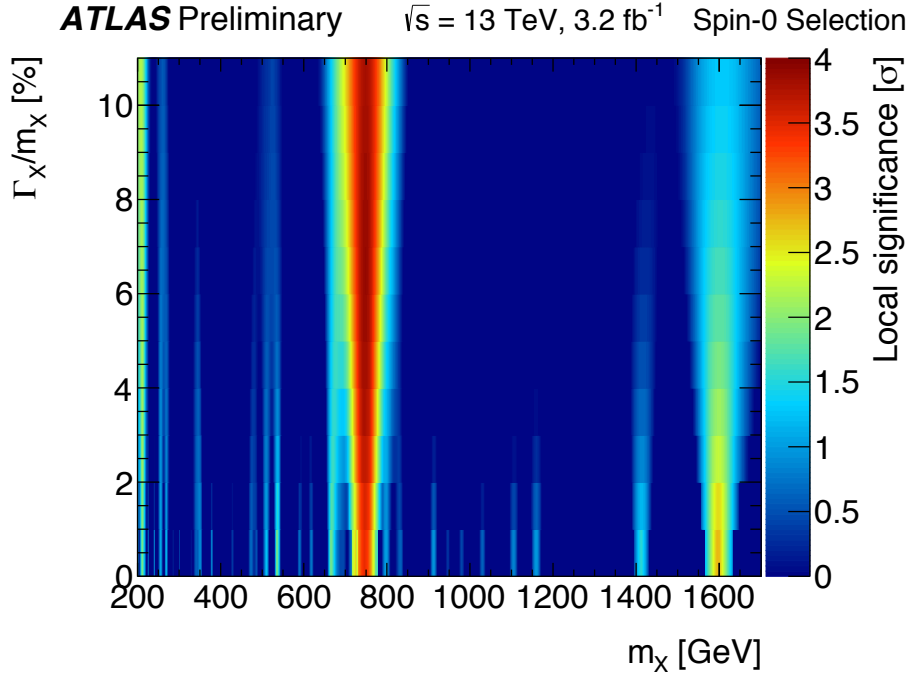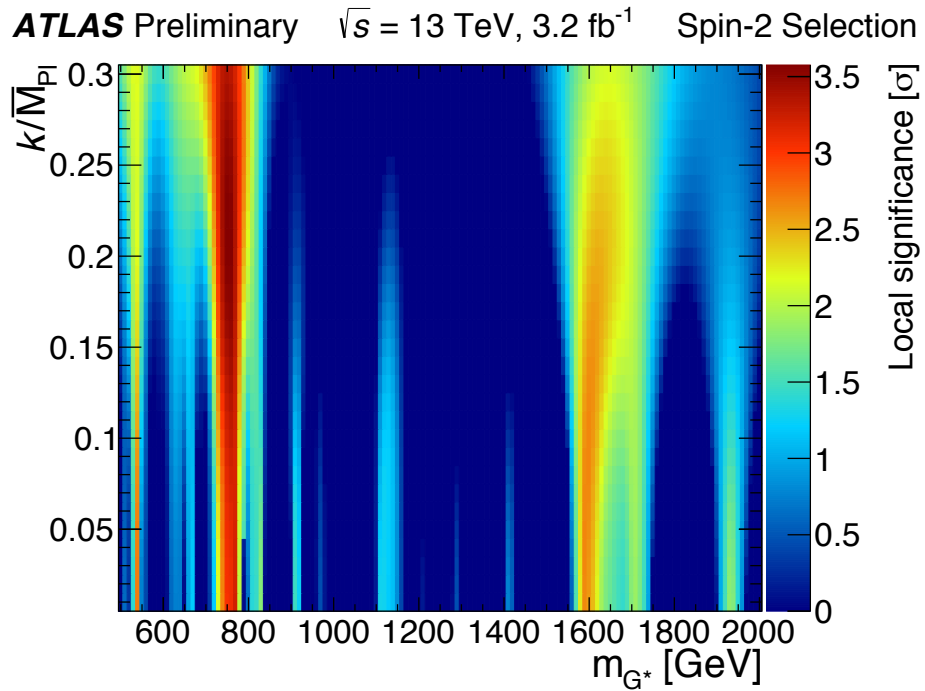
Figure 6: Compatibility with the background-only hypothesis as a function of the assumed signal mass m_X and relative width Γ_X/m_X for the analysis optimized for a spin-0 resonance search.

Figure 7 shows the limits on the signal fiducial cross section as a function of the hypothesized mass for various assumptions on the width. Except near 750 GeV, the observed limit is in agreement with the expected limit assuming the background-only hypothesis. For the relative decay width, Γ_X/m_X, of 1% of the resonance mass, the fiducial cross-section limits range from 50 fb at 200 GeV to 1 fb at 2000 GeV.

8.2 Results of the search for a spin-2 resonance

Figure 8 shows the diphoton invariant mass distribution for the events selected in the spin-2 resonance search together with the best background-only fit (N_S=0). Figure 9 illustrates the local compatibility with the background-only hypothesis as a function of the assumed mass and for various $k/\overline{M}_{Pl}$ values.

As in the spin-0 resonance search, the largest deviation from the background-only hypothesis is observed near a mass of 750 GeV, for a $k/\overline{M}_{Pl}$ value of 0.21, corresponding to a local excess of 3.6 standard deviations and a global significance of 1.8 standard deviations. The width associated to $k/\overline{M}_{Pl} = 0.21$ at $m_{G^*} = 750$ GeV is 48 GeV.

The events selected in the spin-0 search constitute a subset of those selected in the spin-2 resonance search, so the two analyses are not independent. The compatibility between the excesses observed in the two analyses is assessed with a bootstrap statistical procedure, under the assumption of a common signal. If the spin-0 signal is assumed, the two analyses are compatible within 0.02 standard deviations. It is 0.9 standard deviations for the RS graviton signal model.
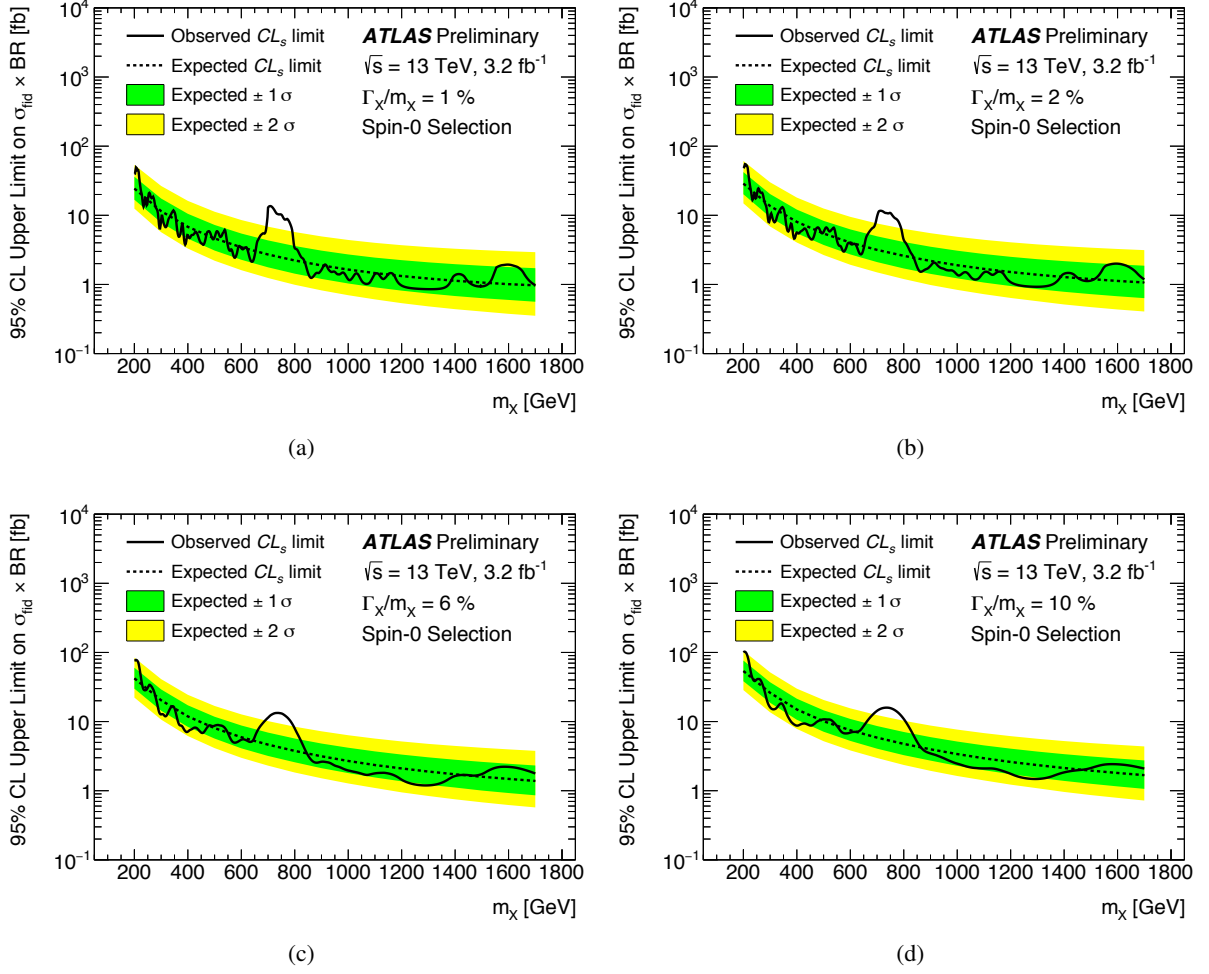
Figure 7: Upper limits on the fiducial cross section at $\sqrt{s}$=13 TeV of a spin-0 particle as a function of the assumed mass m_X, for different values of the decay width divided by the mass.

Figure 10 shows the limit on the benchmark spin-2 RS graviton cross section as a function of mass for different $k/\overline{M}_{Pl}$ values from 0.05 to 0.3. The observed limits on the cross section times branching ratio range from 20 fb to 1 fb for a RS graviton mass between 500 GeV and 3500 GeV for small couplings and 60 fb to 1 fb for $k/\overline{M}_{Pl} = 0.3$, except near the region where the excess is observed. The expected cross-section values in the RS benchmark model for large $k/\overline{M}_{Pl}$ in this mass range are significantly higher.
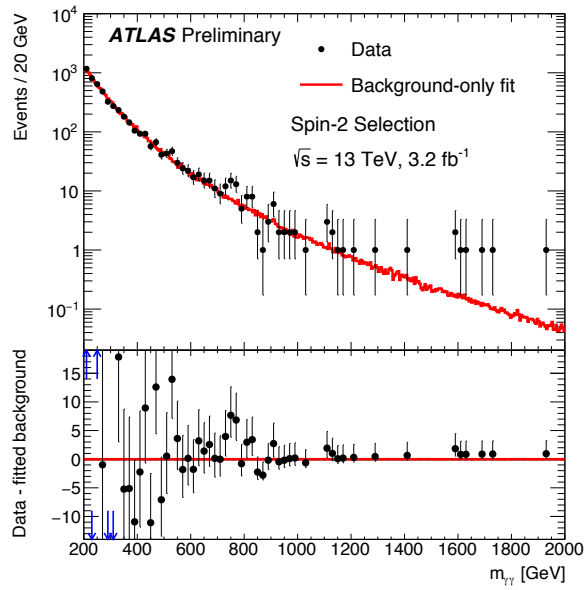
Figure 8: Distribution of the diphoton invariant mass for the selection used in the search for a spin-2 resonance, with the best background-only fit (top). The difference between the data and this fit is shown in the bottom panel. The arrows indicate values outside the range shown in the bottom panel.

Figure 9: Compatibility with the background-only hypothesis as a function of the assumed signal mass and $k/\overline{M}_{\mathrm{Pl}}$ for the spin-2 resonance search.
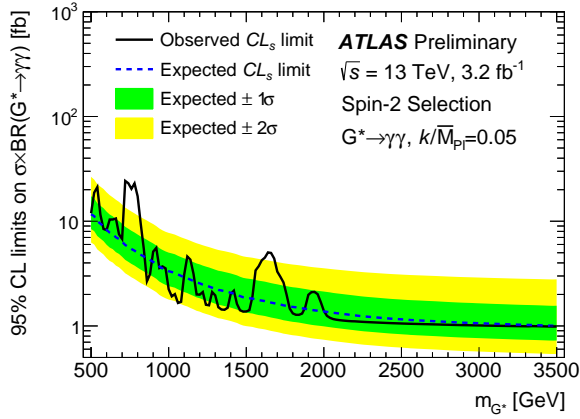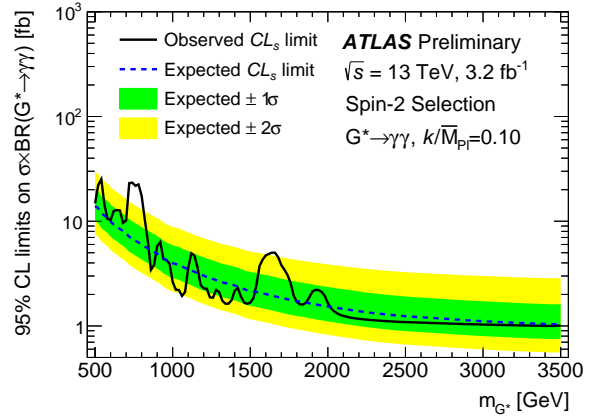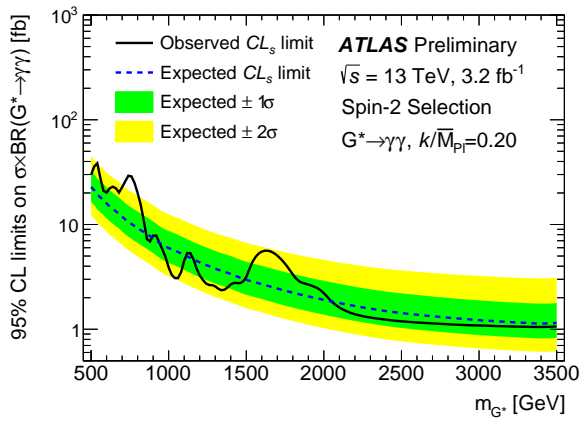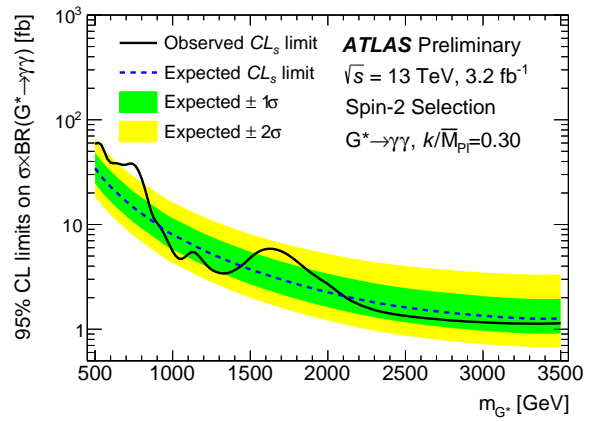
Figure 10: Upper limits on the production cross section of a RS graviton as a function of the assumed mass, for different values of $k/\overline{M}_{Pl}$.

8.3 Kinematic distributions for events $m_{\gamma\gamma}$ around 750 GeV

Several cross-checks of the events with invariant masses near 750 GeV have been performed and no problem related to the photon energy measurement or photon identification and reconstruction has been found. A comparison of the properties of the events is made between the events with $m_{\gamma\gamma}$ in the interval 700-840 GeV and the events in the sideband regions with $m_{\gamma\gamma}$ between 600 GeV and 700 GeV or with $m_{\gamma\gamma}$ larger than 840 GeV. For the selection optimized for the spin-0 (spin-2) resonance search, 31 (70) data events are observed with $m_{\gamma\gamma}$ in the interval 700-840 GeV, 29 (77) in the sideband with 600 GeV$< m_{\gamma\gamma} <$ 700 GeV and 11 (38) in the sideband $m_{\gamma\gamma} >$ 840 GeV. The properties investigated are the number of reconstructed jets, the total transverse momentum of the diphoton system, the magnitude of the missing transverse momentum ($E_{\mathrm{T}}^{\mathrm{miss}}$) and the cosine of the angle between the beam axis and the forward going photon in the Collins-Soper frame [50] of the diphoton system ($\cos(\theta_{\gamma\gamma}^*)$). Jets are reconstructed from calorimeter energy clusters using the anti-k_t algorithm [51] with a distance parameter of 0.4. They are required to have $p_{\mathrm{T}} >$ 25 GeV and $|\eta| <$ 4.4 and to fulfill criteria based on tracking information [52] to reject pileup jets when $p_{\mathrm{T}} <$ 50 GeV and $|\eta| <$ 2.4. The missing transverse momentum is computed as the negative vectorial sum of the transverse momenta of photons, electrons, muons and jets associated to the diphoton vertex and of a soft term [53], accounting for the underlying event and soft radiation, which is constructed using tracks from the primary vertex, not associated with other identified objects. Figures 11 and 12 show the distributions of these properties, for the selections optimized for the spin-0 and spin-2 resonance searches, respectively. The data in the different mass intervals are also compared to the SHERPA predictions for the diphoton background, which represents about 90% of the total number of background events. No significant difference is observed between the different mass regions. Alternative presentations of these distributions are given in the Appendix. In addition, no electron or muon candidates have been found, with $p_{\mathrm{T}} >$ 10 GeV and $|\eta| <$ 2.47 (electrons) or 2.7 (muons) in the events with invariant masses between 700 GeV and 840 GeV. The identification selections of electron and muon candidates correspond to the medium levels [54, 55] with loose isolation criteria.

8.4 Compatibility with 8 TeV data

The 8 TeV pp collision data recorded in 2012, corresponding to an integrated luminosity of 20 fb^{-1}, are re-analyzed with a photon energy calibration as described in Ref. [37], which is close to the calibration used for the 13 TeV data. The selections, including the photon isolation and identification requirements, are the same as in the original publications [13, 15] but the spin-0 resonance search is now also performed at higher invariant masses, covering the region around 750 GeV.

The signal and background are modelled following the same methods as described above and used for the 13 TeV data. The treatment of systematic uncertainties takes into account the correlations between the two datasets from the common photon energy calibration procedure. Figure 13 shows the invariant mass distributions for the two selections.

In the search optimized for a spin-0 resonance, the 8 TeV data show an excess corresponding to 1.9 standard deviations for the hypothesis of a signal of mass 750 GeV and width $\Gamma/M = 0.06$, for which the largest deviation over the background-only hypothesis is observed in the 13 TeV data. In the search optimized for a spin-2 resonance, no excess is observed above the background expectation for the signal hypothesis giving the largest deviation from the background-only hypothesis in the 13 TeV data. This finding is fully consistent with the published analysis [13].
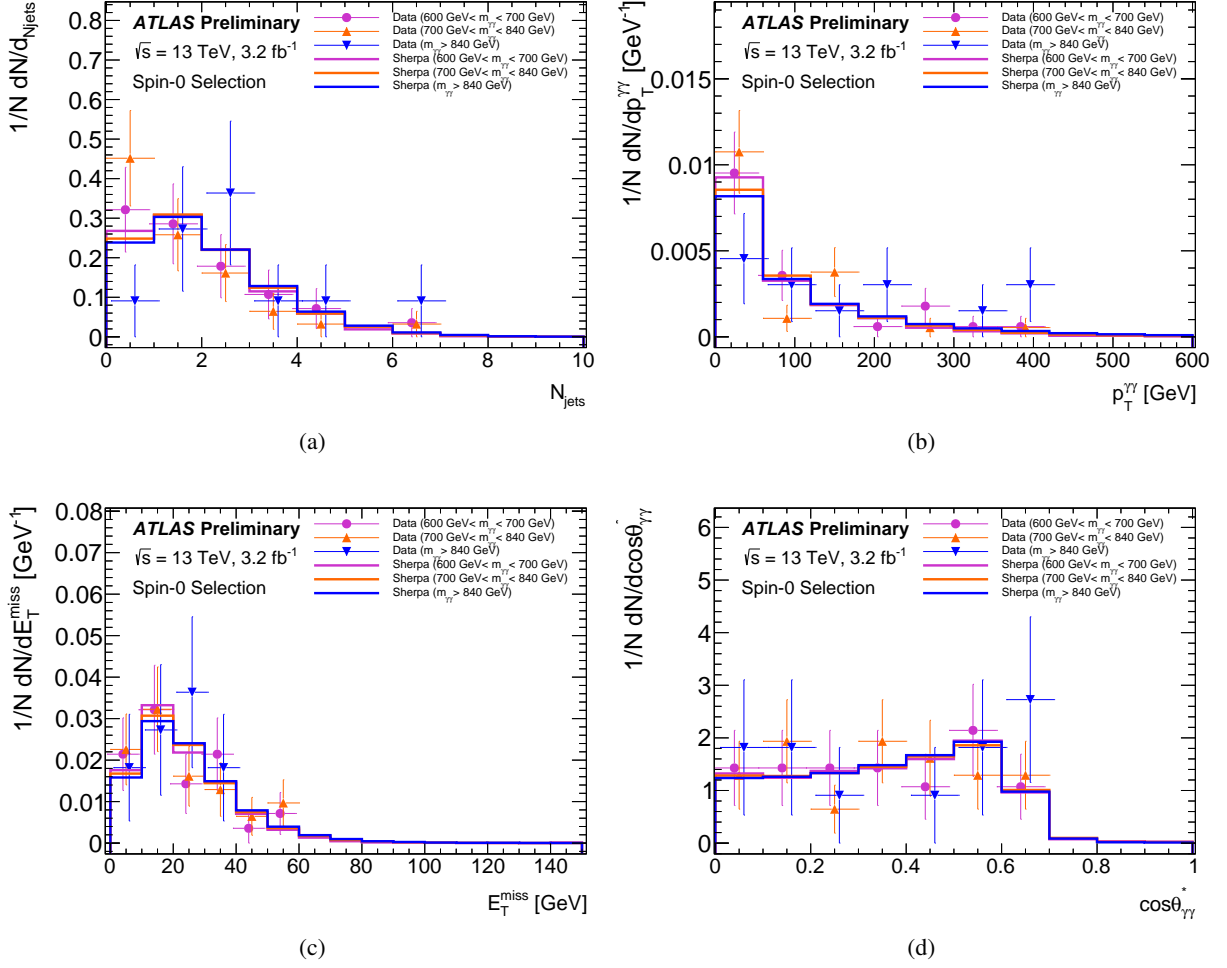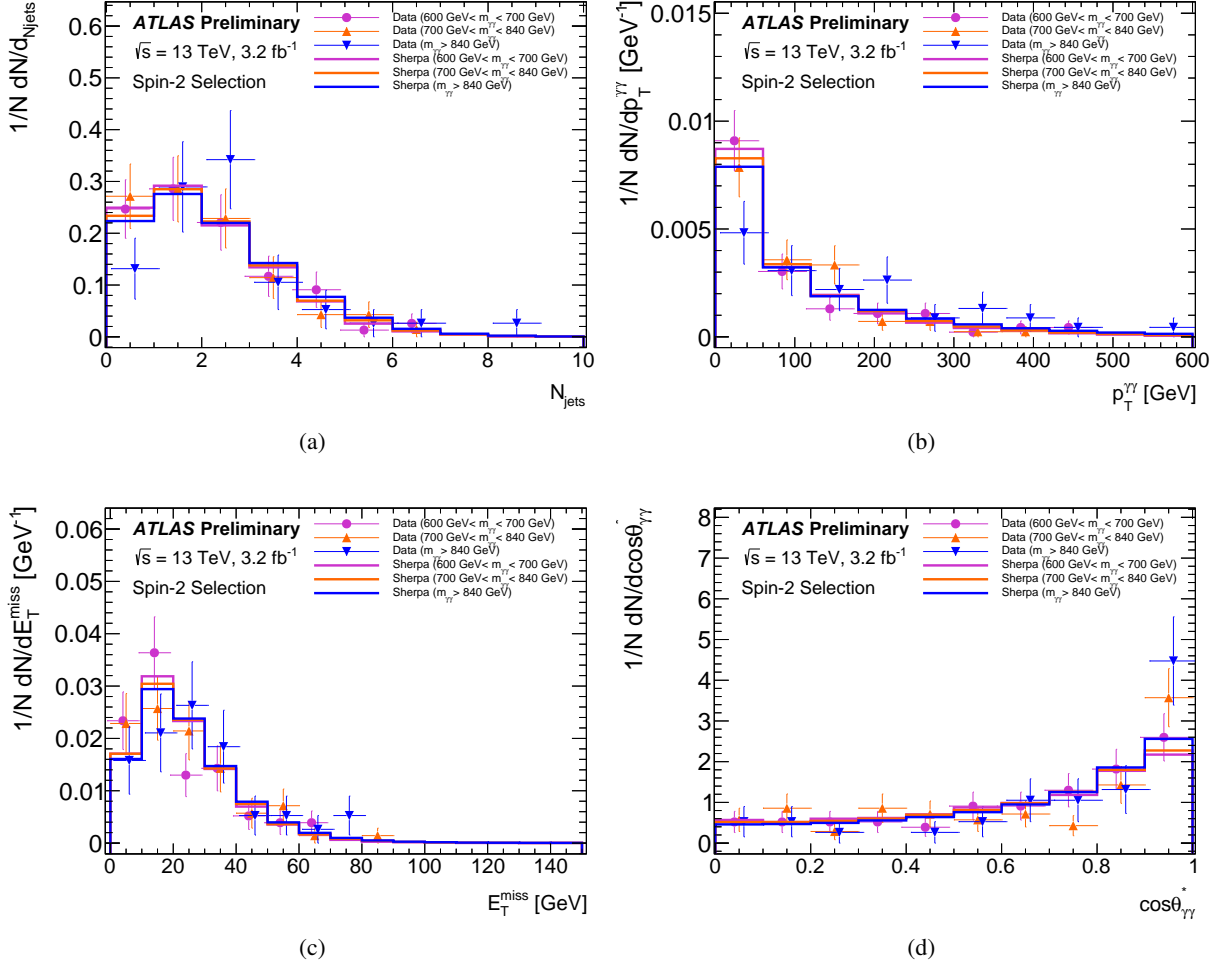
Figure 11: Distributions of (a) the number of jets per event, (b) the transverse momentum of the diphoton system, (c) the missing transverse momentum and (d) $\cos(\theta_{\gamma\gamma}^*)$ for events in the mass interval 700-840 GeV, and the regions 600-700 GeV or > 840 GeV, for events fulfilling the analysis optimized for a scalar resonance search. The SHERPA predictions for the irreducible $\gamma\gamma$ background are also shown. All distributions are normalized to unity.

The consistency of the excess near an invariant mass of 750 GeV between the 8 TeV and 13 TeV datasets is estimated assuming a common signal model. For a particle of mass 750 GeV produced as an *s*-channel resonance, the expected cross section increases by a factor 4.7 for a gluon-gluon initial state and 2.7 for a light quark-antiquark initial state, as estimated with the MSTW2008NLO or NNLO PDF sets [56]. The consistency is quantified by adding an extra modifier to the predicted cross-section ratio, which should be one if the two datasets are consistent, and treating this modifier as the only parameter of interest in the measurement. The best-fit value of this modifier corresponds to a smaller cross section at 8 TeV than expected from the 13 TeV excess.

For the analyses optimized for the spin-0 resonance search, assuming a scalar resonance produced by gluon fusion with $\Gamma/M = 0.06$, the difference between the 8 TeV and 13 TeV results corresponds to a statistical significance of 1.2 standard deviations if gluon-gluon production is assumed and 2.1 standard

Figure 12: Distributions of (a) the number of jets per event, (b) the transverse momentum of the diphoton system, (c) the missing transverse momentum and (d) $\cos(\theta^*_{\gamma\gamma})$ for events in the mass interval 700-840 GeV, and the regions 600-700 GeV or > 840 GeV, for events fulfilling the analysis optimized for a spin-2 resonance search. The SHERPA predictions for the irreducible $\gamma\gamma$ background are also shown. All distributions are normalized to unity.

deviations for quark-antiquark production. For the analyses optimized for the RS graviton signal model, assuming $k/\overline{M}_{Pl} = 0.21$, the difference corresponds to 2.7 standard deviations for gluon-gluon production and 3.3 standard deviations for quark-antiquark production.
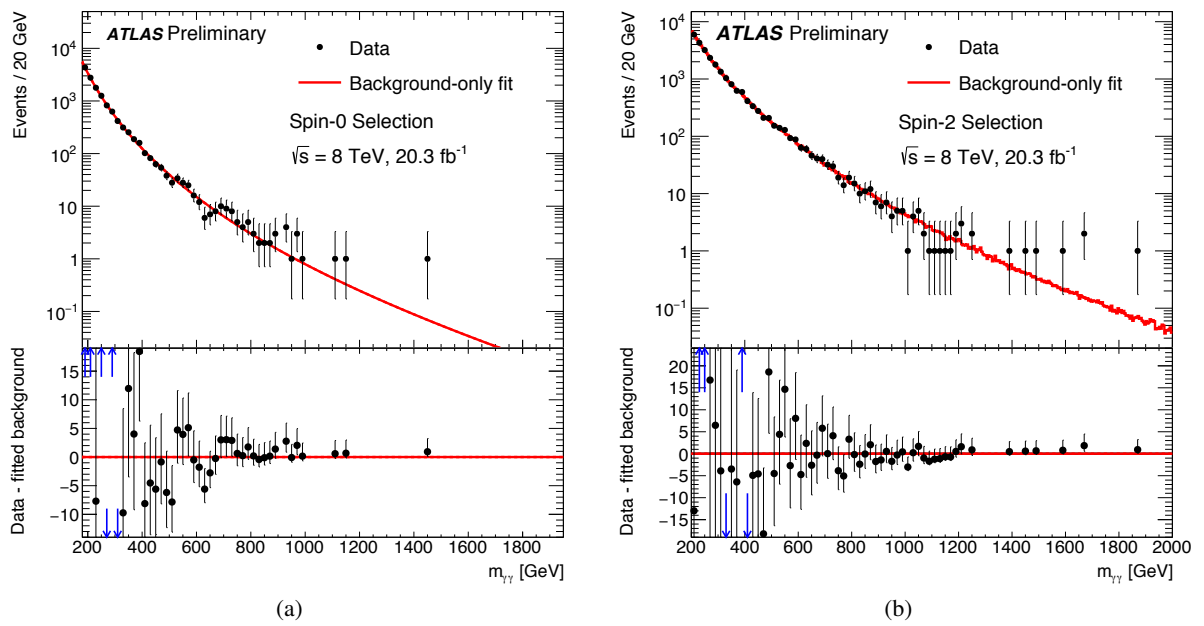
Figure 13: Distribution of the invariant mass of the two photons in the 8 TeV data: (a) for the selection optimized for the search of a spin-0 particle, (b) for the selection optimized for the search of spin-2 particle. The data are compared to the best background-only fit.

9 Conclusion

Searches for new resonances decaying into two photons in the ATLAS experiment at the LHC are presented. The pp collision data corresponding to an integrated luminosity of 3.2 fb^{-1} were recorded in 2015 at a centre-of-mass energy of $\sqrt{s}$ = 13 TeV. Analyses optimized for the search for spin-2 Randall-Sundrum graviton resonances and for spin-0 Higgs-like resonances are performed. The results complement those presented in Ref. [17].

Over most of the diphoton mass range, the data are consistent with the background-only hypothesis and 95% CL limits are derived on the cross section for the production of the two benchmark resonances as a function of their masses and widths. The largest deviation from the background-only hypothesis is observed in a broad region near a mass of 750 GeV, with local significances of 3.6 and 3.9 standard deviations in the searches optimized for the spin-2 and spin-0 resonances, respectively. The global significances are estimated to be 1.8 and 2.0 standard deviations. The results of both analyses are consistent assuming either of the two benchmark signal models. No significant difference is observed in the properties of the events with a diphoton mass near 750 GeV compared to those at higher or lower masses. Assuming a scaling of the production cross section for an s-channel resonance produced by gluon fusion (light quark-antiquark annihilation), the consistency between the 13 TeV data and the data collected at 8 TeV is found to be at the level of 2.7 (3.3) standard deviations using results from the searches optimized for a spin-2 particle and at the level of 1.2 (2.1) standard deviations using results from the searches optimized for a spin-0 particle.

References

[1] L. Randall and R. Sundrum, *A Large mass hierarchy from a small extra dimension*, Phys. Rev. Lett. **83** (1999) 3370, arXiv: `hep-ph/9905221 [hep-ph]`.

[2] T. Appelquist, A. Chodos and P. Freund, *Modern Kaluza-Klein theories*, vol. 65, Frontiers in Physics, Addison-Wesley, 1987.

[3] H. Davoudiasl, J. Hewett and T. Rizzo, *Phenomenology of the Randall-Sundrum gauge hierarchy model*, Phys. Rev. Lett. **84** (2000) 2080, arXiv: `hep-ph/9909255 [hep-ph]`.

[4] A.Hill and J.J.van der Bij, *Strongly interacting singlet - doublet Higgs model*, Phys. Rev. D **36** (1987) 3463.

[5] M. J. G. Veltman and F. J. Yndurain, *Radiative correction to WW scattering*, Nucl. Phys. B **325** (1989) 1.

[6] T.Binoth and J.J.van der Bij, *Influence of strongly coupled, hidden scalars on Higgs signals*, "Z.Physics.C" **75** (1997) 17, arXiv: `hep-ph/9608245 [hep-ph]`.

[7] R. Schabinger and J. D. Wells, *A Minimal spontaneously broken hidden sector and its impact on Higgs boson physics at the large hadron collider*, Phys. Rev. D **72** (2005) 093007, arXiv: `hep-ph/0509209 [hep-ph]`.

[8] B. Patt and F. Wilczek, *Higgs-field portal into hidden sectors* (2006), arXiv: `hep-ph/0605188 [hep-ph]`.

[9] G. M. Pruna and T. Robens, *Higgs singlet extension parameter space in the light of the LHC discovery*, Phys. Rev. D **88** (2013) 115012, arXiv: `1303.1150 [hep-ph]`.

[10] T. D. Lee, *A theory of spontaneous T violation*, Phys. Rev. D **8** (1973) 1226.

[11] ATLAS Collaboration, *Search for extra dimensions in diphoton events using proton-proton collisions recorded at $\sqrt{s}$ = 7 TeV with the ATLAS detector at the LHC*, New J. Phys. **15** (2013) 043007, arXiv: `1210.8389 [hep-ex]`.

[12] CMS Collaboration, *Search for signatures of extra dimensions in the diphoton mass spectrum at the Large Hadron Collider*, Phys. Rev. Lett. **108** (2012) 111801, arXiv: `1112.0688 [hep-ex]`.

[13] ATLAS Collaboration, *Search for high-mass diphoton resonances in pp collisions at $\sqrt{s}$ = 8 TeV with the ATLAS detector*, Phys. Rev. D **92** (2015) 032004, arXiv: `1504.05511 [hep-ex]`.

[14] CMS Collaboration, *Search for high-mass diphoton resonances in pp collisions at $\sqrt{s}$ = 8 TeV with the CMS detector* (2015), CMS-PAS-EXO-12-045.

[15] ATLAS Collaboration, *Search for scalar diphoton resonances in the mass range $65 - 600$ GeV with the ATLAS detector in pp collision data at $\sqrt{s} = 8\,TeV$*, Phys. Rev. Lett. **113** (2014) 171801, arXiv: `1407.6583 [hep-ex]`.

[16] CMS Collaboration, *Search for diphoton resonances in the mass range from 150 to 850 GeV in pp collisions at $\sqrt{s}$ = 8 TeV*, Phys. Lett. B **750** (2015) 494, arXiv: `1506.02301 [hep-ex]`.

[17] ATLAS Collaboration, *Search for resonances decaying to photon pairs in 3.2 fb⁻¹ of pp collision at √s=13 TeV with the ATLAS detector*, ATLAS-CONF-2015-081 (2015), URL: http://atlas.web.cern.ch/Atlas/GROUPS/PHYSICS/CONFNOTES/ATLAS-CONF-2015-081.

[18] CMS Collaboration,
Search for new physics in high mass diphoton events in proton-proton collisions at √s=13 TeV,
CMS-PAS-EXO-15-004 (2015), URL: http://cms-results.web.cern.ch/cms-results/public-results/preliminary-results/EXO-15-004/index.html.

[19] ATLAS Collaboration, *The ATLAS Experiment at the CERN Large Hadron Collider*,
JINST **3** (2008) S08003.

[20] ATLAS Collaboration, *Improved luminosity determination in pp collisions at sqrt(s) = 7 TeV using the ATLAS detector at the LHC*, Eur. Phys. J. **C73** (2013) 2518,
arXiv: 1302.4393 [hep-ex].

[21] T. Sjöstrand, S. Mrenna and P. Z. Skands, *A Brief Introduction to PYTHIA 8.1*,
Comput. Phys. Commun. **178** (2008) 852, arXiv: 0710.3820 [hep-ph].

[22] S.Carrazza, S.Forte and R.Rojo, *Parton Distributions and Event Generators* (2013),
arXiv: 1311.5887 [hep-ph].

[23] ATLAS Collaboration, *ATLAS Pythia 8 tunes to 7 TeV data* (2014),
URL: http://cdsweb.cern.ch/record/1966419.

[24] S. Alioli et al., *A general framework for implementing NLO calculations in shower Monte Carlo programs: the POWHEG BOX*, J. High Energy Phys. (2010) 043, arXiv: 1002.2581 [hep-ph].

[25] E. Bagnaschi et al.,
Higgs production via gluon fusion in the POWHEG approach in the SM and in the MSSM,
J. High Energy Phys. (2012) 088, arXiv: 1111.2854 [hep-ph].

[26] ATLAS Collaboration, *Search for Scalar Diphoton Resonances in the Mass Range 65–600 GeV with the ATLAS Detector in pp Collision Data at √s = 8 TeV*, Phys. Rev. Lett. **113** (2014) 171801,
arXiv: 1407.6583 [hep-ex].

[27] CMS Collaboration, *Search for diphoton resonances in the mass range from 150 to 850 GeV in pp collisions at √s = 8 TeV*, Phys. Lett. B **750** (2015) 494, arXiv: 1506.02301 [hep-ex].

[28] P. Nason and C. Oleari,
NLO Higgs boson production via vector-boson fusion matched with shower in POWHEG,
JHEP **1002** (2010) 037, arXiv: 0911.5299 [hep-ph].

[29] H.-L. Lai et al., *New parton distributions for collider physics*, Phys. Rev. D **82** (2010) 074024,
arXiv: 1007.2241 [hep-ph].

[30] J. Pumplin et al.,
New generation of parton distributions with uncertainties from global QCD analysis,
JHEP **07** (2002) 012, arXiv: hep-ph/0201195 [hep-ph].

[31] ATLAS Collaboration, *Measurement of the Z boson transverse momentum distribution in pp collisions at √s = 7 TeV with the ATLAS detector*, J. High Energy Phys. **2014** (2014) 55,
arXiv: 1406.3660 [hep-ex].

[32] T. Gleisberg et al., *Event generation with SHERPA 1.1*, J. High Energy Phys. **0902** (2009) 007,
arXiv: 0811.4622 [hep-ph].

[33] ATLAS Collaboration, *The ATLAS simulation infrastructure*, Eur. Phys. J. **C70** (2010) 823, arXiv: 1005.4568 [physics.ins-det].

[34] S. Agostinelli et al., *GEANT4: A simulation toolkit*, Nucl. Instrum. Meth. **A506** (2003) 250.

[35] ATLAS Collaboration, *Measurements of the photon identification efficiency with the ATLAS detector using 4.9 fb⁻¹ of pp collision data collected in 2011*, ATLAS-CONF-2012-123 (2012), URL: http://atlas.web.cern.ch/Atlas/GROUPS/PHYSICS/CONFNOTES/ATLAS-CONF-2012-123.

[36] ATLAS Collaboration, *Measurement of the inclusive isolated prompt photon cross section in pp collisions at $\sqrt{s}$ = 7 TeV with the ATLAS detector*, Phys. Rev. D **83** (2011) 052005, arXiv: 1012.4389 [hep-ex].

[37] ATLAS Collaboration, *Electron and photon energy calibration with the ATLAS detector using LHC Run 1 data*, Eur. Phys. J. **C74** (2014) 3071, arXiv: 1407.5063 [hep-ex].

[38] H.Abreu et al, *Performance of the electronic readout of the ATLAS liquid argon calorimeters*, Journal of Instrumentation **5** (2010) P09003, URL: http://stacks.iop.org/1748-0221/5/i=09/a=P09003.

[39] ATLAS Collaboration, *Measurement of the Higgs boson mass from the $H \rightarrow \gamma\gamma$ and $H \rightarrow ZZ^* \rightarrow 4\ell$ channels in pp collisions at center-of-mass energies of 7 and 8 TeV with the ATLAS detector*, Phys. Rev. D **90** (2014) 052004, arXiv: 1406.3827 [hep-ex].

[40] ATLAS Collaboration, *Measurement of isolated-photon pair production in pp collisions at $\sqrt{s}$ = 7 TeV with the ATLAS detector*, JHEP **1301** (2013) 086, arXiv: 1211.1913 [hep-ex].

[41] ATLAS Collaboration, *Measurement of the isolated diphoton cross section in pp collisions at $\sqrt{s}$ = 7 TeV with the ATLAS detector*, Phys. Rev. D **85** (2012) 012003, arXiv: 1107.0581 [hep-ex].

[42] T. Binoth et al., *A full next-to-leading order study of direct photon pair production in hadronic collisions*, Eur. Phys. J. C **16** (2000) 311, arXiv: hep-ph/9911340 [hep-ph].

[43] P. M. Nadolsky et al., *Implications of CTEQ global analysis for collider observables*, Phys. Rev. D **78** (2008) 013004, arXiv: 0802.0007 [hep-ph].

[44] T. Aaltonen et al., *Search for new particles decaying into dijets in proton-antiproton collisions at $\sqrt{s}$ = 1.96 TeV*, Phys. Rev. D **79** (11 2009) 112002, URL: http://link.aps.org/doi/10.1103/PhysRevD.79.112002.

[45] ATLAS Collaboration, *Measurement of Higgs boson production in the diphoton decay channel in pp collisions at center-of-mass energies of 7 and 8 TeV with the ATLAS detector*, Phys. Rev. D **90** (2014) 112015, arXiv: 1408.7084 [hep-ex].

[46] G. Cowan et al., *Asymptotic formulae for likelihood-based tests of new physics*, Eur. Phys. J. C **71** (2011) 1554, [Erratum: Eur. Phys. J.C73,2501(2013)], arXiv: 1007.1727 [physics.data-an].

[47] E. Gross and O. Vitells, *Trial factors or the look elsewhere effect in high energy physics*, Eur. Phys. J. C **70** (2010) 525, arXiv: 1005.1891 [physics.data-an].

[48] O. Vitells and E. Gross, *Estimating the significance of a signal in a multi-dimensional search*, Astropart. Phys. **35** (2011) 230, arXiv: `1105.4355 [astro-ph.IM]`.

[49] A. L. Read, *Presentation of search results: The CL$_s$ technique*, J. Phys. **G28** (2002) 2693.

[50] J. C. Collins and D. E. Soper, *Angular distribution of dileptons in high-energy hadron collisions*, Phys. Rev. D **16** (7 1977) 2219.

[51] G. P. S. M. Cacciari and G. Soyez, *The Anti-k(t) jet clustering algorithm*, J. High Energy Phys. **04** (2008) 063, URL: `http://dx.doi.org/10.1088/1126-6708/2008/04/063`.

[52] ATLAS Collaboration, *Tagging and suppression of pileup jets with the ATLAS detector*, ATLAS-CONF-2014-018, 2014, URL: `http://cdsweb.cern.ch/record/1700870`.

[53] ATLAS Collaboration, *Expected performance of missing transverse momentum reconstruction for the ATLAS detector at $\sqrt{s}$ = 13 TeV*, ATL-PHYS-PUB-2015-023, 2015, URL: `http://cdsweb.cern.ch/record/2037700`.

[54] ATLAS Collaboration, *Electron identification measurements in ATLAS using $\sqrt{s}$ = 13 TeV data with 50 ns bunch spacing*, ATL-PHYS-PUB-2015-041, 2015, URL: `http://cdsweb.cern.ch/record/2048202`.

[55] ATLAS Collaboration, *Muon reconstruction performance in early $\sqrt{s}$ = 13 TeV data*, ATL-PHYS-PUB-2015-037, 2015, URL: `http://cdsweb.cern.ch/record/2047831`.

[56] A. Martin et al., *Parton distributions for the LHC*, Eur. Phys. J. C **63** (2009) 189, arXiv: `0901.0002 [hep-ph]`.

Appendix

Figures 14 and 15 show the distributions of the number of jets per event for the spin-0 and spin-2 selections. The normalized distributions in the data in the three $m_{\gamma\gamma}$ intervals (600-700 GeV, 700-840 GeV and > 840 GeV) are shown separately and compared to the SHERPA predictions for the diphoton background. Figures 16 and 17 show the transverse momentum of the diphoton system, Figures 18 and 19 the missing transverse momentum and Figures 20 and 21 the distributions of $\cos(\theta_{\gamma\gamma}^*)$.
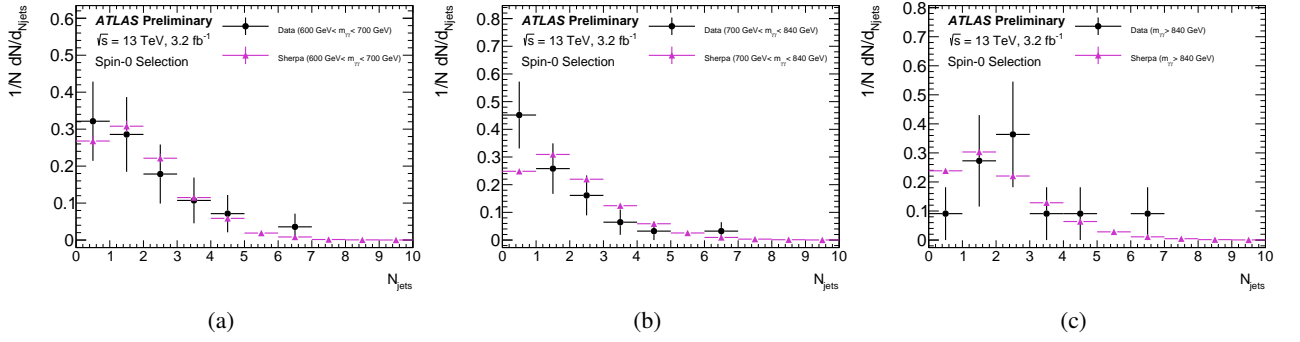
Figure 14: Distributions of the number of jets in the event for the spin-0 selection and (a) the mass interval 600-700 GeV, (b) the mass interval 700-840 GeV and (c) mass > 840 GeV. The SHERPA predictions for the irreducible $\gamma\gamma$ background are also shown. All distributions are normalized to unity.
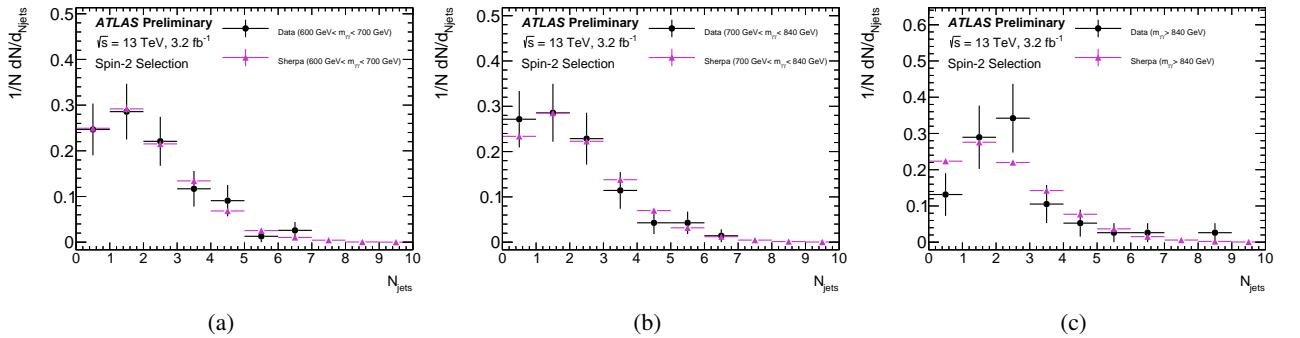
Figure 15: Distributions of the number of jets in the event for the spin-2 selection and (a) the mass interval 600-700 GeV, (b) the mass interval 700-840 GeV and (c) mass > 840 GeV. The SHERPA predictions for the irreducible $\gamma\gamma$ background are also shown. All distributions are normalized to unity.
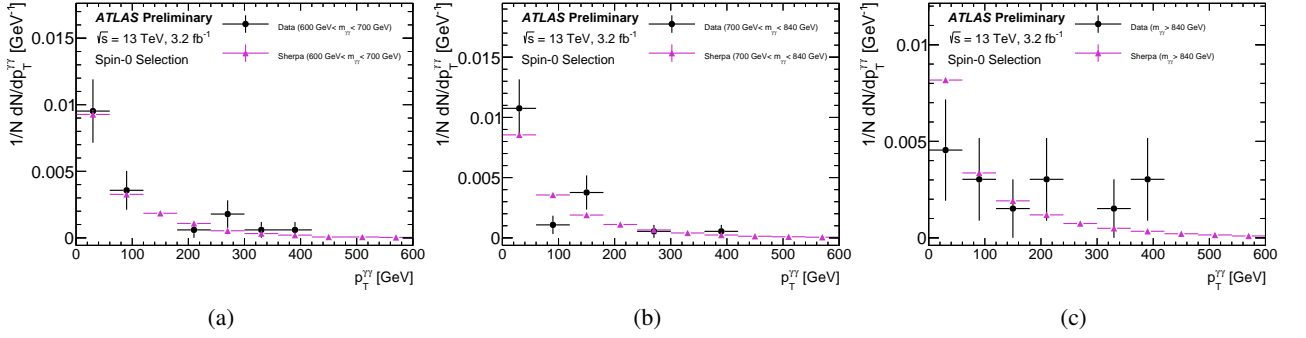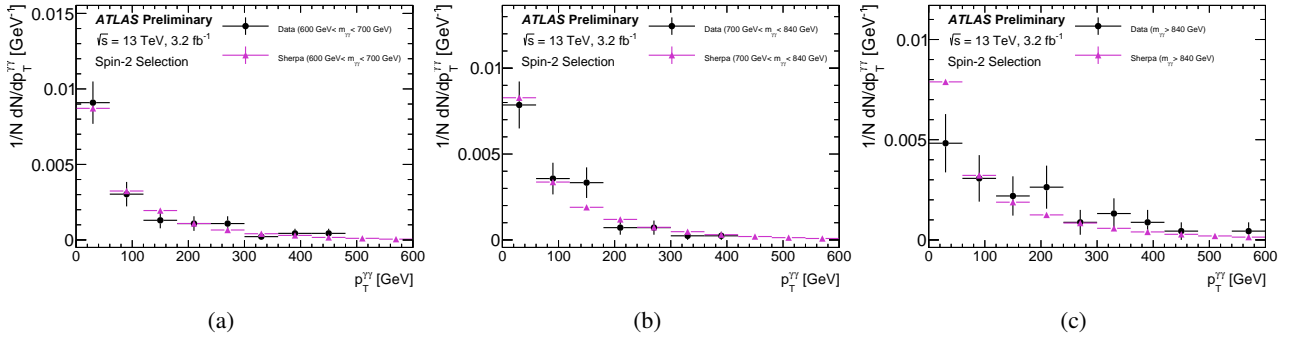
Figure 16: Distributions of the transverse momentum of the diphoton system for the spin-0 selection and (a) the mass interval 600-700 GeV, (b) the mass interval 700-840 GeV and (c) mass > 840 GeV. The SHERPA predictions for the irreducible $\gamma\gamma$ background are also shown. All distributions are normalized to unity.

Figure 17: Distributions of the transverse momentum of the diphoton system for the spin-2 selection and (a) the mass interval 600-700 GeV, (b) the mass interval 700-840 GeV and (c) mass > 840 GeV. The SHERPA predictions for the irreducible $\gamma\gamma$ background are also shown. All distributions are normalized to unity.
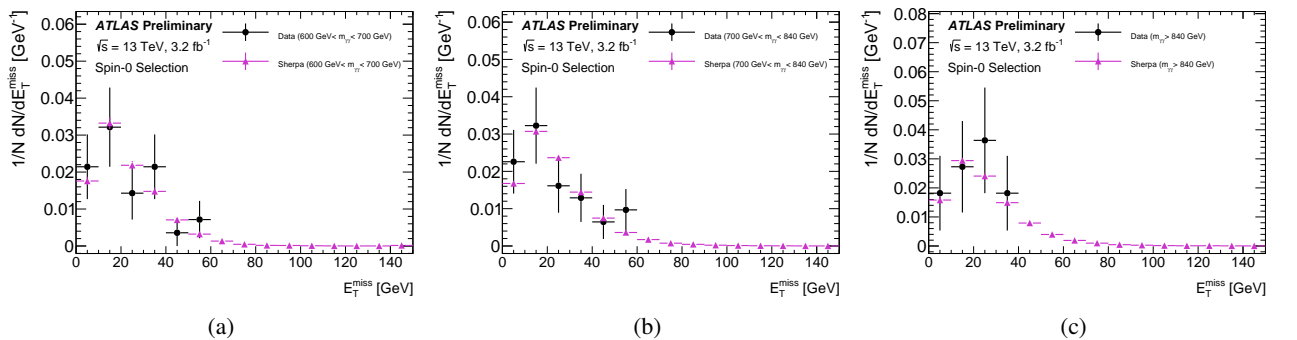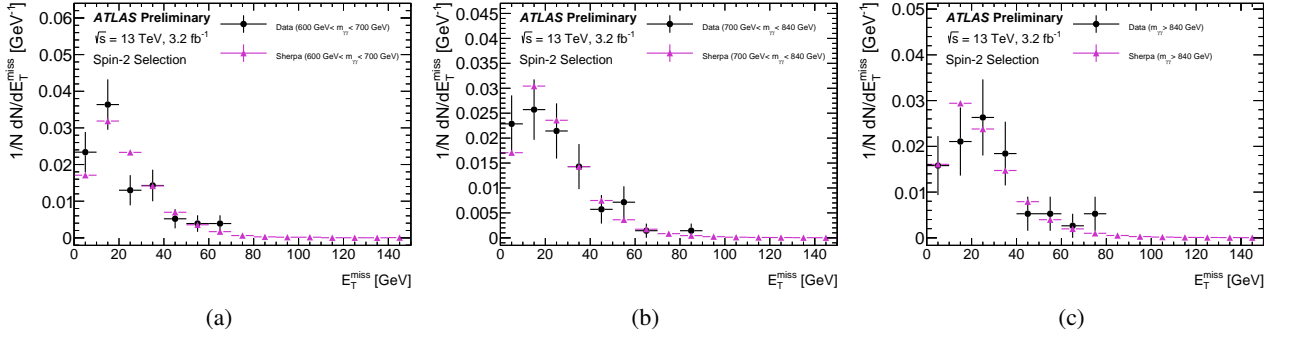

Figure 18: Distributions of the missing transverse momentum for the spin-0 selection and (a) the mass interval 600-700 GeV, (b) the mass interval 700-840 GeV and (c) mass > 840 GeV. The SHERPA predictions for the irreducible $\gamma\gamma$ background are also shown. All distributions are normalized to unity.

Figure 19: Distributions of the missing transverse momentum for the spin-2 selection and (a) the mass interval 600-700 GeV, (b) the mass interval 700-840 GeV and (c) mass > 840 GeV. The SHERPA predictions for the irreducible $\gamma\gamma$ background are also shown. All distributions are normalized to unity.
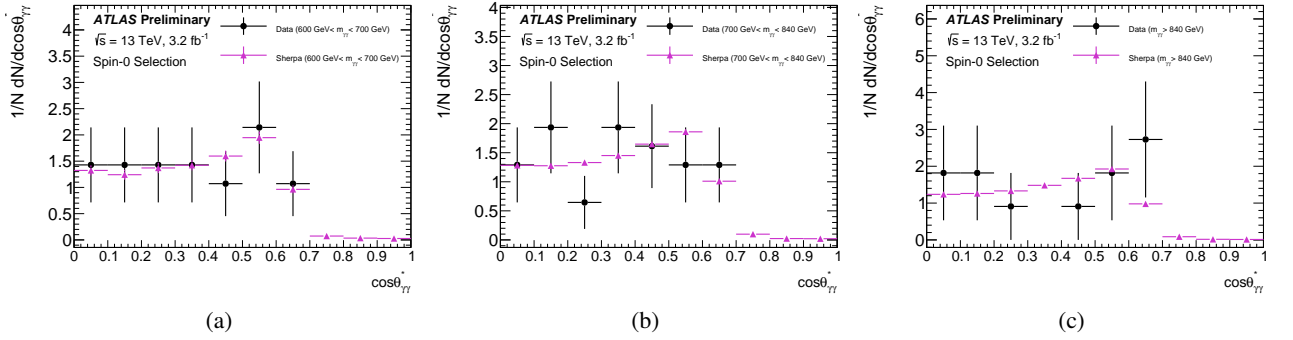

Figure 20: Distributions of $\cos(\theta^*_{\gamma\gamma})$ for the spin-0 selection and (a) the mass interval 600-700 GeV, (b) the mass interval 700-840 GeV and (c) mass > 840 GeV. The SHERPA predictions for the irreducible $\gamma\gamma$ background are also shown. All distributions are normalized to unity.
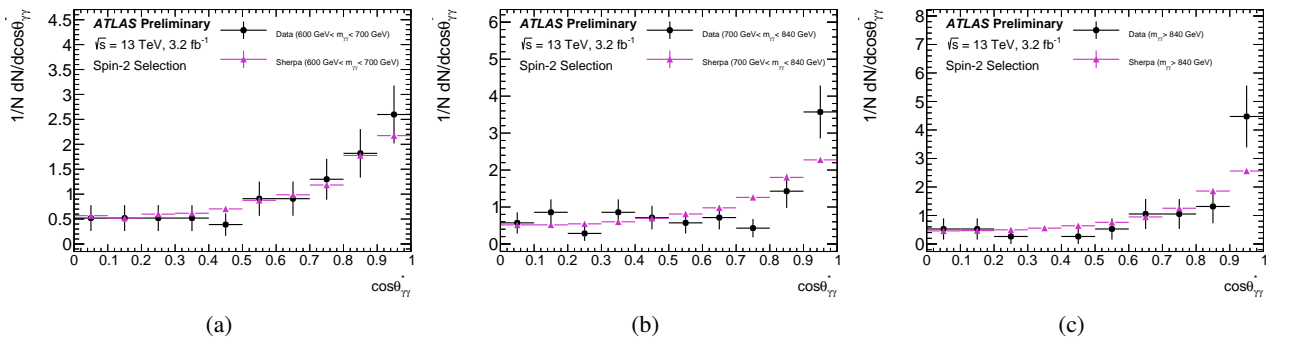

Figure 21: Distributions of $\cos(\theta^*_{\gamma\gamma})$ for the spin-2 selection and (a) the mass interval 600-700 GeV, (b) the mass interval 700-840 GeV and (c) mass > 840 GeV. The SHERPA predictions for the irreducible $\gamma\gamma$ background are also shown. All distributions are normalized to unity.